STUDY OF THE BIREFRIENGENCE OF BLACK PHOSPHORUS BY PICOSECOND INTERFEROMETRY

A THESIS

SUBMITTED TO THE FACULTY OF

UNIVERSITY OF MINNESOTA

BY

WEI ZHENG

IN PARTIAL FULFILLMENT OF THE REQUIREMENTS

FOR THE DEGREE OF

MASTER OF SCIENCE

ADVISOR: XIAOJIA WANG

May 2017

Acknowledgements

First and foremost, my thanks and appreciation go to my advisor, Xiaojia Wang. She fully supported me during my establishment in the academic research and helped me develop rigorous research ethnics and sophisticated research styles. The knowledge that she brought to me in the field of micro-nano scale thermal transfer and radiation is inspiring, and she taught me the critical thinking skill so I can better prepare myself for my career.

The study in this thesis will not complete without the inspiring discussion and help from my research colleagues at Micro-Nano Thermal Transport Lab (MNTTL): Dr. Jie Zhu, Dr. Hu Zhang, Mr. Xuewang Wu, and Mr. Dustin Lattery. Thank you for helping me in understanding nanoscale thermal transport and TDTR technique, which was completely a new field of study to me when I started my graduate school life. I appreciate all your help during my process in studying and exploring the anisotropic properties of black phosphorus and developing my research style.

I would also like to thank Dr. Peipei Wang from the Department of Physics at South University of Science and Technology of China, Shenzhen, China. His skill in fabricating high quality single crystalline black phosphorus makes my study of black phosphorus more fluent. In addition, I would also like to thank Dr. Delin Zhang from the Department of Electrical and Computer Engineering at the University of Minnesota. He helped me with coating black phosphorus samples so that my sample can be measured by picosecond interferometry. Lastly, I would like to thank Professor Tony Low and Professor Rusen Yang for serving as committee members of my final defense.

I enjoy my time at the University of Minnesota Twin Cities. I would like to thank John Gardner and Chris Hogan, who also gave me guidance in accomplishing my Master of Science degree.

Dedication

This thesis is dedicated to my parents, Kefeng Zheng and Xiaohong Huang, who have been providing me with all the supports I needed and are the sole reason that I have such precious opportunities to improve myself by pursuing the M.S. degree. My dearest friends Xin Tong and Ruiyuan Tang, thank you for accompanying me during my time abroad in the US; I am proud to be your best friend.

ABSTRACT

This thesis presents a modified picosecond interferometry method to study the optical properties of bulk black phosphorus (BP). BP is an emerging two-dimensional material which exhibits great potential for use in future nano-photonic and nano-electronic devices. BP differentiates itself from other two-dimensional materials such as graphene in that it possesses anisotropy in in-plane direction. It has zigzag and armchair in-plane crystalline direction, which gives its unique optical and electrical properties along these two directions, and the interlayers are under Van der Waals interactions. BP has direct band gap which is tunable via controlling the number of layers, strain and the applied electric field, making it a versatile material for use in semi-conductor industry. Currently, BP has been used as few-layer materials for devices such as photodetector and field effect transistor. However, the studies on the bulk optical properties of BP are still lacking, partially due to its tendency to degrade when exposed to air. This work focused on presenting picosecond interferometry as a new method for indirectly measuring the optical properties of BP and discuss the extended application of picosecond interferometry for studying other two-dimensional materials.

Picosecond interferometry is a modified pump-probe method. It observes Brillouin scattering in a crystalline system to measure the optical and acoustic properties of the crystalline system. In this study, I modified the pump-probe system in our laboratory into a polarization-sensitive picosecond interferometry setup. I studied BP’s birefringent optical properties at several different wavelengths using picosecond interferometry. The Brillouin scattering signals was modelled by exponential decaying function. The polarization-resolved optical properties of BP were extracted by fitting the exponential decaying function. The thermal backgrounds of the measurement is analyzed with computational simulation.

Table of Contents

List of Figures

List of Symbols

Λ	Thermal conductivity
λ	Laser wavelength
v	Speed of sound
R	Reflectivity
T	Temperature
n	Real part of dielectric constants
κ	Imaginary part of dielectric constants
η	Acoustic strain
ϕ	Phase shift
θ_p	Incident light polarization angle
θ	Angle between the zigzag crystalline orientation and the linear polarization direction
t	Time delay
α	Absorption coefficient
f	Oscillation frequency

Chapter 1 Introduction

1.1 Motivation

Black phosphorus (BP) is the stable form of phosphorus at room temperature. Discovered about 100 years ago [1], its stability is superior compare to other phosphorus allotropes [2]. However, its potentials to be used in semiconducting devices was not recognized by academy and industry until the breakthrough in research on graphene in 2004 [3]. Since then, two-dimensional materials, including few layer BP, have drawn attentions of researchers who are looking for applying the unique properties of two-dimensional materials in the next generation nano-devices [4, 5]. BP can be synthetically fabricated by various methods [6] in the form of bulk single crystal. Bulk BP can be exfoliated by various methods into monolayer or few layers [7-9] and used in nano-devices and studied as thin-film samples.

Black phosphorus is a semiconductor with unique properties unlike any other semiconductors currently available. It has a direct band gap of 0.3 eV in bulk form; for a single layer BP the band gap energy is 2 eV. The bandgap of BP can be tuned by adjusting the number of layers and the relationship between bandgap energy and the number of layer largely remains linear[10]. Figure 1 shows the crystalline structure of BP. BP has an orthorhombic crystalline structure with zigzag and armchair crystalline structure in the in-plane directions, and the interlayers of BP are under Van der Waals interactions. Each layer is estimated to have thickness of 0.6 nm [11]. The orthorhombic crystalline structure has granted BP many of its anisotropic properties [12-15]. Tao *et al.* reported the distinct in-plane Young's modulus of 58.6 GPa along zigzag crystalline direction and 27.2 GPa along the armchair crystalline direction [16]. Zhu *et al.* has discovered that BP has anisotropic thermal conductivities along all three crystalline directions using TR-MOKE. The thermal conductivities are from 84 W m^{-1} K^{-1} to 101 W m^{-1} K^{-1} along the zigzag direction, from 26-36 W m^{-1} K^{-1} along the armchair direction, and around 5 W m^{-1} K^{-1} along the inter-layer direction [17]. Li *et al.* measured the polarization-resolved light absorption of BP at wavelength of 1.5 μm with the incident light normal to the in-plane direction. They discovered that BP has anisotropic light absorption with the largest (smallest) light absorption is achieved when the linearly polarized light polarization direction is aligned along the armchair (zigzag) direction [18]. Xia *et al.* performed angle-resolved DC conductance measurement on BP along various in-plane directions. They reported that BP exhibits strong in-plane anisotropic DC conductance [12]. The combination of BP's unique physical properties makes it a promising material for future generation nano-photonic and nano-electronic devices.

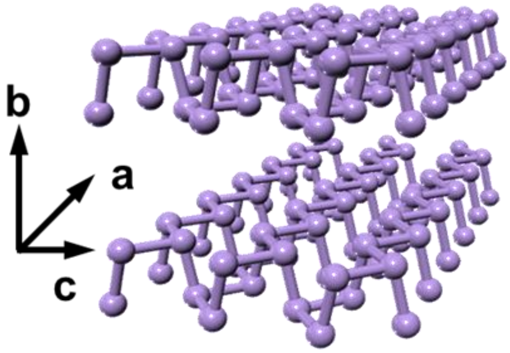

Figure 1. The crystalline structure of BP. The crystalline directions are labeled as zigzag (ZZ) (a), interlayer (b) and armchair (AM) (c). The interlayer spacing is estimated to be 0.6 nm in thickness, and it can be considered as bulk BP when the total thickness exceeds 100-200 nm.

For this master thesis, I will present my research project on understanding the anisotropic properties of BP using picosecond (ps) interferometry technique. The ps interferometry setup is modified from the ultrafast pump-probe system currently available in my laboratory. The Brillouin scattering signal from BP is captured *via* ps interferometry, and a bi-exponential decay model is developed to extract the anisotropic polarization-resolved optical properties of BP. This technique provides BP with adequate protection against the oxidation caused by ambient environment, therefore providing more accurate optical properties data. The optical absorption data would benefit future application of BP such as in BP-based field-effect transistors (FET) and photodetectors.

1.2 Literature Review

Until this day, there has been a number of interests in understanding the fundamentals of BP's unique physical properties. Experimental measurements had been done to measure the optical, electrical, and thermal properties of BP. There have been attempts to understand BP's properties *via* various theoretical modeling. Notable nano-devices such as BP-based FETs and photodetectors had been developed in the past few years with promising performances [19-21]. It has also been discovered that BP has coupling effects with strain and the applied electric field. Its properties can be tuned by applying strain and electric field in the in-plane and through-plane directions [22-24].

Schuster *et al*. had studied the optical response of bulk BP by applying electron energy loss spectroscopy (EELS) in transmission [25]. EELS in transmission is a bulk-sensitive technique that accounts the electron energy loss in scattering with a loss function

[26]. By utilizing apparatus similar to transmission electron microscopy (TEM), electron beam are sent through the sample and some electrons are experiencing inelastic scattering [27]. The energy loss of electrons is captured by electron spectrometer and the cause of energy loss is analyzed [28]. The amount of energy loss at different frequencies is registered and one can determine the types of atoms and the number of atoms presented in the sample. They studied a bulk BP sample of thickness about 100-200 nm, which estimated to be corresponding to 160-300 layers of BP. By maintaining the sample at T = 20 K, they prevented thermal broadening and then measured the EELS intensity along the ZZ and AM directions. They used Kramers-Kronig analysis to retrieve the dielectric function ε_1 and ε_2 along the ZZ and AM directions from EELS measurements. The result shows that BP is highly anisotropic with the highest absorption of infrared and visible spectra in the AM direction.

Attempts to measure BP's optical response with conventional approaches were also made. Tran *et al.* had measured optical absorption spectrum for monolayer, bilayer, tri-layer, and bulk BP with incident light polarized along the ZZ and AM directions [10]. The dielectric constants ε_1 and ε_2 were obtained from the optical absorption spectrum measurement. For monolayer, bilayer and tri-layer BP samples, they discovered that electron-hole interaction has a strong effect on the absorption spectra and it deviates greatly away from the single particle optical absorption spectra. The reason is that excitonic effects take dominance in the few-layer structure and that significantly reshapes the optical spectra. They found that the reduced dimensionality and the depressed screening are the primary contributor for the enhanced excitonic effects. For bulk BP, the excitonic effects are almost negligible. They observed the strongest absorption along the AM direction, which agrees with the EELS measurement done by Schuster *et al*. The highest absorption for the AM direction is observed at infrared and near infrared spectra. The highest absorption for the ZZ direction is observed at the visible and ultraviolet spectra. The highly anisotropic optical nature of BP makes it an ideal linear polarizer that can be used in liquid crystal display and polarized three-dimensional systems [29, 30].

Due to its unique crystalline structure, BP exhibits anisotropic transport and mechanical properties as studied by Tao *et al* [16]. They determined the crystalline directions of a 14.8-nm thick few-layer BP flake by reflectance difference microscopy [10, 31]. They placed a BP flake on SiO_2/Si substrate, then patterned it into an L-shape sample by electron-beam lithography. Each branch of the L-shape samples corresponds to the ZZ and the AM orientations of BP. They measured the anisotropic transport properties of this L-shape BP. They measured the conductance anisotropy to be 63.7%, which agrees well with reference data [32]. The *I-V* curve measured from the sample was used to derive the carrier mobility of 392 and 247 $cm^2\ V^{-1}\ s^{-1}$ for AM and ZZ directions, respectively. In addition to the anisotropic conductance measurement, they also performed bending test on the cantilevers using the AFM bending method [33-35]. The Young's modulus was measured to be 58.6 ± 11.7 GPa for ZZ direction, and 27.2 ± 4.1 GPa for AM direction. On average, the Young's modulus for ZZ direction is 2.2 times higher than that of the AM direction. However, the dependency of mechanical strength on the number of layers contained in the BP flake was not clearly observed. The Young's modulus of BP decreases for approximately 14.6% from bi-layer to monolayer. For thicker material, the change in Young's modulus becomes less obvious due to the weak interlayer Van der Waals interaction, which agrees with the conclusion drawn from the first-principles DFT calculations carried out by Wei *et al* [36]. The breaking stress of the BP flake was measured to be 4.22 GPa and 2.21 GPa for the ZZ and AM directions, respectively, and the breaking strain was measured to be 6.5% and 7.2% for ZZ and AM directions, respectively.

Similar to the technique of Tao *et al.*, Xia *et al.* had fabricated BP device to measure the DC electrical conductance [12]. In their research, BP flakes with 4 to 60 layers (2 to 30 nm in thickness) were used for relative extinction spectrum measurement, DC conductance and Hall mobility measurements along various in-plane directions. The relative extinction spectra reveal that the highest (least) light absorption occurs when the incident light polarization is aligned near AM (ZZ) crystalline direction. The spectra contain a sharp raise at wavenumber of 2400 cm^{-1} which corresponds to a band gap energy of 0.3 eV, a result that agrees well with previous studies on BP [37]. They found that BP exhibits anisotropic in-plane conductance and Hall mobility. The AM conductance is about 1.5 times higher than the ZZ conductance, and the AM Hall mobility is about 1.8 times higher than the ZZ Hall mobility. They also found that the BP Hall mobility exhibits a strong dependence on the number of layers and temperature [38, 39].

There were many theoretical prediction on BP transport and optical properties. Qiao *et al.* [13] used a combination of density function (DFT) theory, carrier mobility calculation and absorption spectrum calculation [40-44] to predict the structural information, carrier mobility, and optical absorption spectra of 1-5 layers and bulk BP. From their theoretical prediction, the BP carrier mobility varies from 600 to 6400 $cm^2\ V^{-1}\ s^{-1}$ depending on the number of layers. The in-plane electron and hole mobility are moderately anisotropic, but the holes are more mobile than electron in both ZZ and AM crystalline directions. They found that carrier mobility in the AM direction is almost twice of that in the ZZ direction, with the exception of monolayer case. The prediction also shows that BP exhibits linear dichroism as discussed in other literature [12, 25].

Low *et al.* discussed the tunability of BP optical properties under different doping, thickness, and polarization [45]. Using the Kubo formula [22], the real part of optical conductivities along the AM direction $\mathrm{Re}(\sigma_{xx})$ and the ZZ direction $\mathrm{Re}(\sigma_{yy})$ were calculated for different sample thickness, doping, and polarization angles. It was predicted that for a 10-nm BP thin film, $\mathrm{Re}(\sigma_{xx})$ is higher than $\mathrm{Re}(\sigma_{yy})$ and $\mathrm{Re}(\sigma_{xx})$ increases with increasing thickness from 4 nm to 20 nm. Their calculated polarization dependent absorption agrees with the previous optical measurements [12], suggesting highly anisotropic optical response of BP.

Fei *et al.* had demonstrated *via* first-principles simulation that BP exhibits coupling effect between strain and carrier mobility [14]. Their simulation result suggested that by applying in-plane uniaxial and biaxial strains on monolayer or bilayer BP, it is possible to rotate the preferred electrical conducting direction by 90 degrees from the AM to ZZ direction. According to this work, for monolayer BP, a 6% uniaxial strain along the ZZ crystalline direction could change the preferred conducting direction from AM to ZZ. They predicted that the same effect could be achieved if a 4% biaxial strain is applied.

Black phosphorus had been used in nano-devices, of which the most notably are the BP-based field-effect transistors (FETs) and waveguide-integrated photodetectors [19, 46, 47]. Buscema *et al.* fabricated few-layer BP (3-8 nm thick) FETs. The BP layer acted as gate for this FET [48]. Their measurement estimated that the BP hole mobility and the electron mobility were ~100 $cm^2 V^{-1} s^{-1}$ and ~0.5 $cm^2 V^{-1} s^{-1}$, respectively. These values deviated largely from previous measurements [12, 16], however they only represented the lower bound of BP mobility, since the measurement included the contact resistance of the FETs. They measured the FET photoresponse performance. They found that, unlike other 2D material-based FETs that can only operate in the visible and ultraviolet spectra [49-52], the BP FET can be excited at wavelength up to 940 nm, making it an ideal candidate for FETs that require responsiveness at near-infrared spectrum. They reported that the FETs responsivity decreased as the laser wavelength increases, which implied that BP has more optical absorption at shorter wavelengths. They predicted, based on the measurements, that the responsivity cutoff wavelength was around 997 nm. This cutoff wavelength is higher than the previously reported values for other two-dimensional materials [53-55]. This prediction suggested that BP-based photonic devices have more applications at longer wavelength. The responsivity dropped as the incident light power increased following a power law of $R \propto {P_d}^{\alpha - 1}$ where α is approximately 0.7. The drop in responsivity was also observed in other photodetectors [50, 51] as result of reduced carriers under high photon flux [56]. Their device response rise and fall time were measured to be 1 ms and 4 ms respectively, which was remarkable when compared with other two-dimensional material-based photodetectors [53, 54, 57].

A waveguide-integrated BP based photodetector is developed by Nathan *et al.* [47]. They fabricated a BP FET onto a silicon waveguide with few-layer graphene serving as the top gate. The responsivity of their BP photodetector increased as the device bias voltage increased, and the responsivity increased with increasing BP flake thickness. The dark current of this BP photodetector was measured to be 220 nA and the normalized photocurrent to dark current ratio is 85 mW^{-1}, which outperformed the graphene photodetectors under the same testing conditions [58-60].

In summary, the unique physical properties of BP have drawn immense interests of study and nano-device applications. The optical, electrical, thermal, and mechanical properties of BP had been studied by many researchers using distinct experimental methods. Theoretical predictions on BP's electrical properties, band structure, and lattice constants had been performed. BP-based nano-devices, although not prevalent, had been developed to serve photonic, electrical and thermal applications [61-63]. However, experimental studies on BP remains difficult. For BP optical property measurements, the degradation of BP in ambient environment makes it challenging to capture reliable measurement results. The past optical experiments focused mainly on few-layer BP and there lacks experimental results on bulk BP. In this work, the polarization-resolved optical absorption of BP is measured by a modified ps interferometry method. The ps interferometry method is a non-contact technique to indirectly measure the optical properties of BP. The modified ps interferometry has several advantages over the conventional optical spectroscopy [64]. Firstly, the BP is coated with metal transducer to prevent degradation when exposed to air. Secondly, it allows polarization-resolved optical property measurement. Lastly, unlike the conventional optical spectroscopy method, it can extract the dielectric constants of the BP flake without knowing the sample thickness, therefore reducing input data uncertainty. The modified ps interferometry method provides accurate and reliable optical measurement results that will benefit the design and fabrication of the next generation nano-photonic devices.

1.3 Thesis Outline

This thesis is composed of five chapters. In chapter 2, the BP sample fabrication and the basics time-domain thermoreflectance (TDTR) measurement technique is explained. The necessary modification to upgrade TDTR for ps interferometry measurement is also discussed. I also explained the ps interferometry measurement technique. In chapter 3, the general theoretical foundations of ps interferometry are discussed first. Then specifically for my BP sample system, the generation of acoustic wave and the consequential Brillouin scattering in BP is explained in detail. Lastly, the method of data reduction to extract the polarization-resolved BP optical absorption property is explained in detail. Chapter 4 discusses my results of the ps interferometry experiments. Further, the optical properties measured from ps interferometry are compared with literature values. A combination of electromagnetic and thermal computational simulation is performed to analyze the anomalous thermal background. Chapter 5 summarizes the work that I have completed during my Master study and highlights the potential future research directions based on my study.

Chapter 2 Experimental Methods

2.1 General Methodology

In this thesis, I used ps interferometry modified from time-domain thermoreflectance (TDTR) to measure the optical properties bulk BP with thickness on the order a few microns. Picosecond interferometry observes Brillouin scattering [65, 66] to study the acoustic wave generation and attenuation inside BP. Brillouin scattering signal can be used to extract the optical constants of the birefringent BP. Based on the ps interferometry experimental methods previously developed by Thomsen *et al.* [67, 68], I modified the TDTR system in the my laboratory (Micro-Nano Thermal Transport Lab, MNTTL) at the University of Minnesota into a ps interferometry system to measure the polarization-resolved optical properties of BP at wavelength of 783 nm, 835 nm and 890 nm.

In a previous study on the anisotropic thermal conductivity of BP [17] by Zhu *et al.*, time resolved magneto-optic Kerr effect (TR-MOKE) technique was used to measure BP thermal conductivities. During the TR-MOKE measurement, a weak Brillouin scattering signal was also observed. The Brillouin scattering signal was weak and only last less than 100 ps time delay. The relatively weak Brillouin signal was due to (1) MOKE was not sensitive in detecting phonon propagation and attenuation; and (2) the thicker magnetic transducer (~30-nm Terbium Iron, TbFe) absorbed over 50% of the light, only a small fraction of light entered BP was scattered by acoustic wave. In order to magnify the Brillouin scattering signal, I upgraded the standard TDTR system to a ps interferometry system. A half waveplate was added to the system for adjusting light polarization direction. The two optical short pass filters were removed from the system in order to extend the measurement wavelength range. I also prepared the BP samples by exfoliating BP crystals and sputtering a thin film of 5-nm Pt on to the BP flake. The thin transducer provides several functions: (1) it launches an acoustic wave into the BP flake, which causes Brillouin scattering; (2) it avoids BP degradation when BP is exposed to air. One advantage of such a sample system is that the optical absorption coefficient extraction is insensitive to the thickness uncertainty of the BP flake. Picosecond interferometry can provide more accurate optical constants data (n and κ) over the conventional optical spectroscopy [64]. In addition, ps interferometry can probe the optical constants of the sample simultaneously in one measurement, while the conventional optical spectroscopy measurements require separated reflection measurement and transmission measurement. Also, ps interferometry uses very confined laser beam spots [69], making it an ideal approach for measuring thin film samples on the micron lateral size. For the rest of the chapter, I will present the details on sample preparation, the basics of TDTR and the ps interferometry system I used for Brillouin scattering measurements.

2.2 Sample Preparation

Throughout the process of my study, three samples were fabricated: 5-nm Pt on BK-7 glass (5-nm Pt/BK-7), 5-nm Pt on BP (5-nm Pt/BP) and 20-nm TbFe on BP (20-nm TbFe/BP). I used the 5-nm Pt/BK-7 glass sample as a reference, and measured the 5-nm Pt/BP and the 20-nm TbFe/BP samples and compared their results. The BP was synthesized with a low pressure technique [70] by our collaborator Peipei Wang from department of physics at University of Science and Technology of China. A mixture of 60 mg Sn (Alfa Aesar, 99.85%), 30.6 mg Snl4 (Alfa Aesar, 99.998%) and 1.5 g red phosphorus (Alfa Aesar, 98.9%) was vacuum sealed inside a quartz tube. The tube was maintained at 650 °C in a furnace for one hour, followed by a cooling process to 300 °C with a temperature decreasing rate of 0.22 °C per minute for 26.2 hours. During this process, single crystalline BP flakes are grown. The X-ray diffraction (XRD) inspection of BP proves that the single crystalline BP is of high quality, the peaks found in the XRD matches the PDF card of BP as shown in Fig. 2.2 (A), showing the high quality of the BP sample.

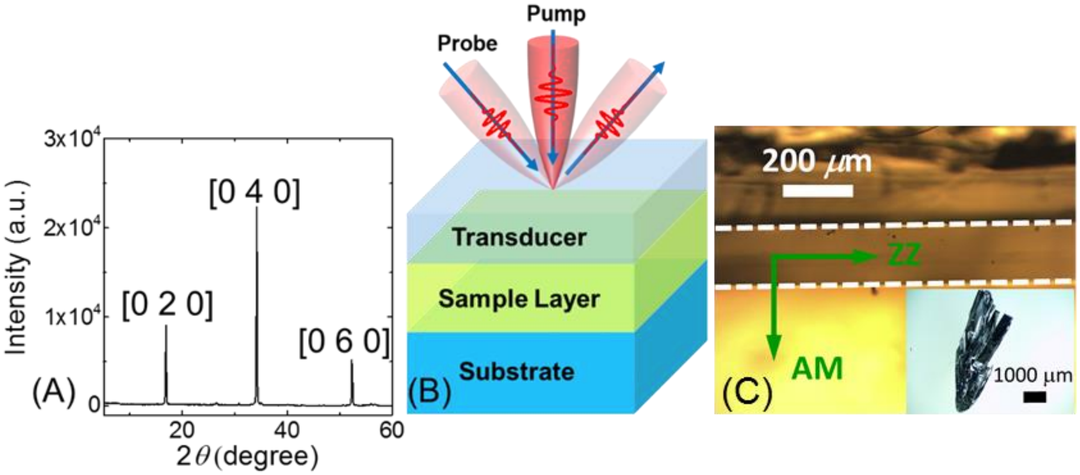

Figure 2.2. (A) The XRD 2θ scan of the BP sample. The peaks correspond the [0 2 0], [0 4 0] and [0 6 0] crystalline plane, indicating the high quality of the BP flake. (B) A typical sample stack for ultra-fast laser pump-probe measurement. The sample to be studied (green layer) is deposited onto a substrate (blue layer) with high thermal conductivity. A layer of metal transducer is deposited on top of the sample layer. (C) Microscopic image of a small BP ribbon (indicated between the blue dashed lines) that is mechanically exfoliated from bulk single crystalline BP (shown by the inset). The arrows indicates the ZZ and AM crystalline directions. In this study, ZZ is defined as 0^o and AM is defined as 90^o.

For ultra-fast laser pump-probe measurements, a typical sample stack is shown in Fig. 2.2(B). A layer of metal transducer is required for both TDTR and ps interferometry measurements. The TDTR measurement requires an optically-opaque transducer (~100-nm), which absorbs photon energy and delivers thermal energy into the sample beneath. In ps interferometry, thinner transducer (~10-nm) is required for launching an acoustic wave into the sample layer. In this study, small BP ribbon was mechanically exfoliated from the bulk single crystalline BP flake, which is shown in the microscopic image in Fig. 2.2(C). The thickness of the exfoliated BP ribbon is on the order of tens of microns. Due to its unique crystalline structure, BP shows a needle-like shape with the longer edge along the ZZ direction. The exfoliated BP ribbon was adhered to silicon substrate by thermally conductive tape to maximize thermal transport from the BP sample to the substrate. The BP/Si stack was coated with metal transducer in sputtering chamber. Since BP is prone to oxidation degradation, the BP was sealed in vacuum before sputtering. Once the coating is done, the BP flake is isolated from air thus prevented from oxidation degradation.

In order to verify that the ps interferometry setup work properly, I prepared a 5-nm Pt/BK-7 glass reference. The literature values of BP-7 glass's optical and acoustic properties are available. By measuring the properties of BK-7 glass and compare the results with literature values, I verified the reliability of the ps interferometry. The verification result is presented in chapter 3.

2.3 Basic Time-Domain Thermoreflectance (TDTR) and TDTR based Picosecond Interferometry

Time-Domain thermoreflectance is a well-developed all-optical measurement technique used to monitor the transient temperature change of a thin film. The measurement data can be used to extract the thermal properties of the thin film by fitting the experimental data to a transient thermal model [69, 71, 72]. TDTR belongs to the general pump-probe technique family, in which, the pump beam serve as the optical excitation of the transducer film and cause its temperature rise. The probe beam is reflected from the metal surface and received by a fast-response Si-based photodetector. The heat absorbed by the metal transducer conducts into the sample and substrate (if presents), therefore the transducer surface temperature decays. Due to the effect known as thermoreflectance (see below), the reflectivity of the metal transducer will change as temperature decays. The reflected probe beam intensity also contains such changes proportional to the transducer temperature. Thus, the variation in the probe beam intensity reflected from the sample is related with its temperature change.

Thermoreflectance is defined as the relationship between the change in reflectivity and the temperature change of a material. As temperature of the material changes, the refractive index of the material also changes, therefore causes a change in reflectivity ΔR . For common metallic material such as Aluminum or Pt, the relationship can be approximated as first order linear within a small temperature range (typically less than 10 K). The relationship can be described by the equation [73]

$$\frac{\Delta R}{R} = \left(\frac{1}{R} \frac{\partial R}{\partial T} \right) \Delta T = k \Delta T \tag{2.1}$$

where k is the thermoreflectance coefficient. The thermoreflectance coefficients for metals are small, typically on the order of 10^{-5} ~ 10^{-4} per degree Kelvin, and are wavelength dependent [72]. Therefore, advanced techniques are needed in order to collect and analyze the low-level measurements. A frequency-sensitive resonance circuit, a pre-amplifier, a phase-sensitive lock-in amplifier, and double-modulation of the pump and probe beams are used to improve the signal-to-noise ratios for reliable measurements.

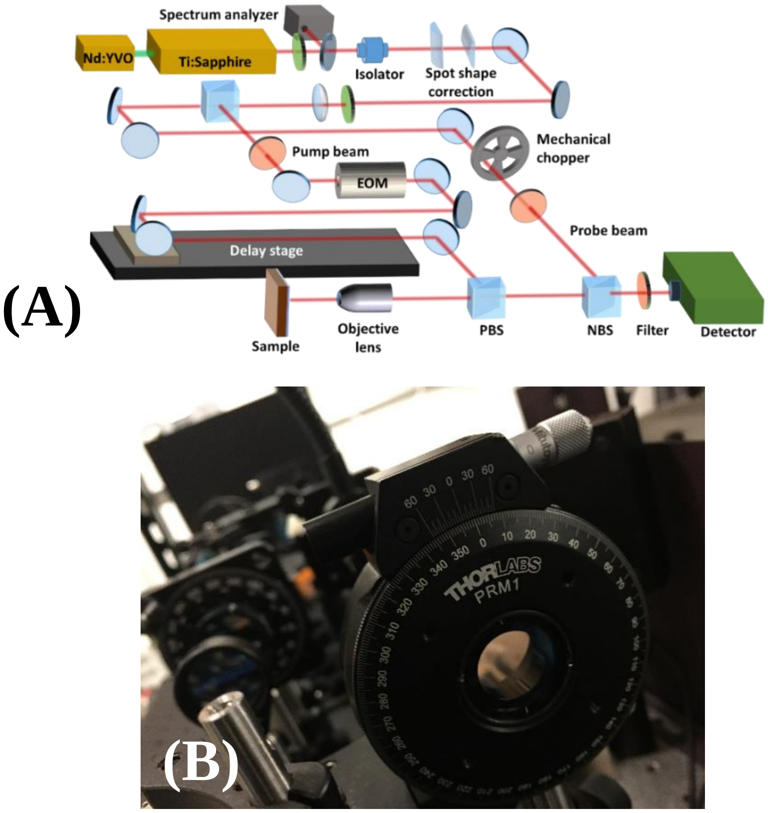

Figure 2.3.1. (A) The schematic diagram showing all the major parts of the TDTR setup. (B) A close-up loop at the half waveplate mounted on a high precision rotational mount used in the ps interferometry experiment to manipulate the incident probe beam polarization orientation.

Figure 2.3.1(A) shows the schematic diagram of the TDTR system used in MNTTL. A Ti:Sapphire ultra-fast laser system is used to produce laser pulses at frequency 80 MHz. A non-polarizing beam splitter (NBS) directs a small amount of the laser towards a spectrum analyzer in order to check the status of the pulse laser. Typically, the laser wavelength is centered at 783 nm with 13 nm full-width half maximum (FWHM) pulse width. The duration between two laser pulses is 12.5 ns.

The laser beam passes through an isolator, which utilizes the faraday rotation effect to prevent reflected laser beam from returning to the Ti:Sapphire system, which could interfere with the normal operation of the Ti:Sapphire system. Spot shape correction lenses are used to reshape the laser beam to be circular, and the laser beam is separated by a polarizing beam splitter (PBS) into pump beam and probe beam. The pump beam is sent through a long pass optical filter and the probe beam is sent through a short pass optical filter. The pump beam, which passes through an electro-optic modulator (EOM), is being modulated at designated radio frequency, typically between 1 MHz and 18 MHz. The modulated frequency is determined by sensitivity analysis of the experiment. The probe beam is modulated by a mechanical chopper at an audio frequency of 200 Hz. This is known as the double-modulation for low-level signal collection.

After the pump and the probe beams are modulated, the probe beam is directed onto the sample and focused by an objective lens. The pump beam needs to travel through an additional delay stage. The retroreflector on the delay stage can move back and forth, adjusting the total optical path difference between the pump beam and the probe beam. This creates a time delay between the pump heating and probe sensing. By controlling this optical path difference, one can measure the change in temperature as a function of time delay, therefore obtain the transient temperature change profile of the metal transducer. For ps interferometry, a half waveplate as shown in Fig. 2.3.1(B) was added between the objective lens and the PBS to change the laser polarization direction.

The pump beam pulses excite the sample metal transducer surface, rise the temperature of the sample metal transducer therefore changing its reflectivity. The probe beam arrives at the metal transducer at a controlled time delay after the arrival of pump beam pulses. The time-dependent reflected probe beam intensity is recorded by the photodetector. In order to prevent pump beam from entering the photodetector and interfere with probe beam signal collection, a short pass filter is placed before the photodetector to remove pump beam. The signal from photodetector is amplified for further analysis. The signal has a real component V_{in} and an imaginary component V_{out}. The V_{in} signal is related with the temperature change at the transducer, and the V_{out} signal is related with the phase of the signal and heat accumulation during measurement.

Figure 2.3.2(A) shows the V_{in} signal obtained from the 70-nm Al/ 300-nm SiO_2/ bulk Si reference sample. The initial sharp jump in V_{in} resulted from the sudden temperature rise upon the arrival of pump beam onto the sample transducer surface. The optical penetration depth of the laser (calculated by $\delta = 1/4\pi k\eta_0$) is 7.38 nm at 783 nm, therefore the Aluminum film is optically opaque. The cooling corresponds to the decay in V_{in} signal as time delay increases. The V_{out} signal is shown in Fig. 2.3.2(B). I took the ratio V_{in}/V_{out} because the noise in V_{in} and V_{out} will cancel out. I fitted the ratio with a thermal model as shown in Fig. 2.3.2(C). The thermal model requires inputs of thickness, thermal conductivity and heat capacity of each individual layer (except for the sample thermal conductivity to be determined from measurements), the beam spot size, laser power and modulation frequency. For this reference sample measurement, the thermal conductivity of the 300-nm SiO_2 layer was fitted to be 1.36 W/m-K, which agrees with the literature value [74]. This result verified the accuracy and reliability of our TDTR system.

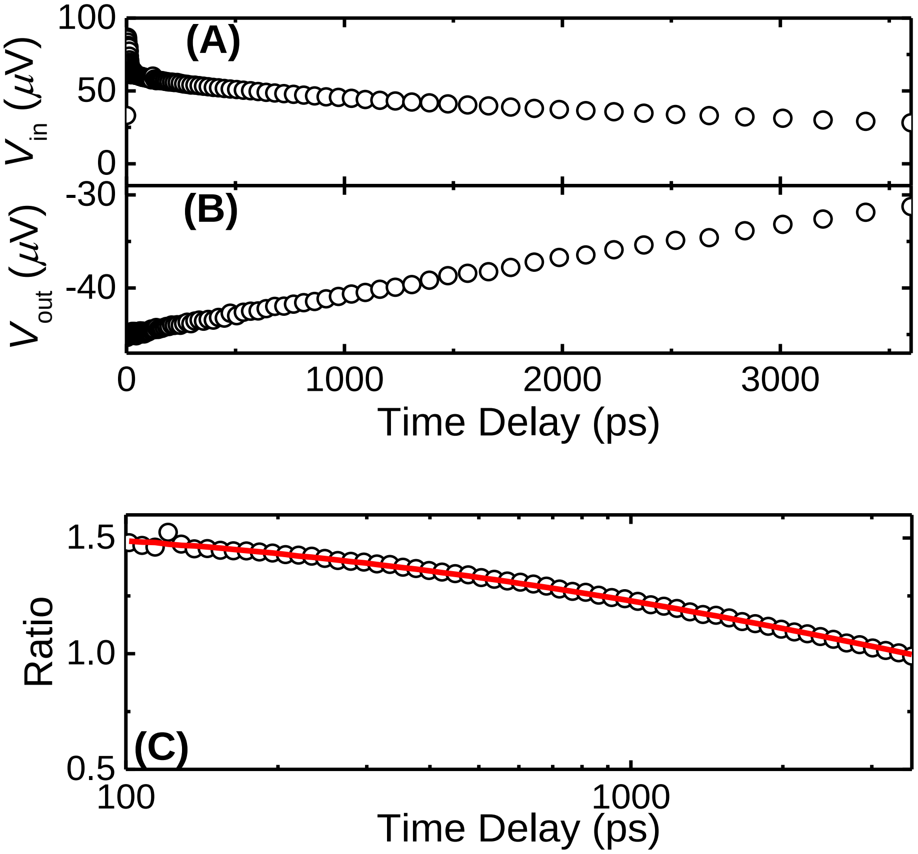

Figure 2.3.2 The TDTR signal obtained from the 70-nm Al/300-nm SiO_2/bulk Si wafer sample. (A) The real part of the signal V_{in}. The valley at 21 ps indicates the acoustic echo of the Al film, which is used to calculate and verify the Al film thickness [69]. The inset shows the TDTR signal over 3600 ps time delay range. (B) The imaginary part of the signal V_{out}. (C) The fitting of ratio signal V_{in}/V_{out}. Open circles are experimental data; the red solid line is the fitting curve.

In order to modify the TDTR setup to accommodate ps interferometry for measuring BP, changes must be made to both the sample transducer and the TDTR system.

Firstly, the key idea of ps interferometry is to launch acoustic waves into the sample *via* laser heating of the transducer, meanwhile the metal transducer is semi-transparent. Secondly, the measurement system can change the probe beam incident polarization angle to gather polarization-resolved data from birefringent BP. Lastly, the optical filters in the TDTR system limited measurement wavelength at 783 nm, therefore modification is needed to extend the measurement range to longer wavelength.

I calculated the optical penetration depth δ of TbFe and Pt to be 18.73 nm and 7.90 nm, respectively. The optical penetration depth δ_{TbFe} was calculated using the optical properties of Fe as a lower bound since the optical properties of TbFe alloy was not available. The optical penetration depth δ_{Pt} is less than the 5 nm Pt film thickness, therefore, it allows laser to penetrate through the Pt transducer. The transfer matrix method [75] calculation revealed that at least 20% of laser energy penetrates through the metal transducers, leading to highly observable Brillouin scattering signals in BP. In addition, the transfer-matrix method estimated that about 50~60% laser energy is absorbed by the metal transducers. This causes considerable thermal deformation of the transducer, which launches strong acoustic waves into the BP sample.

To enable the incident-light polarization control in our ps interferometry system, I added a half waveplate mounted on a high precision rotational mount before the objective lens. The minimum rotational increment of the mount is 1°; each rotation increment produces a 2° rotation in polarization angle.

At last, the optical layout of the TDTR system needs to be modified in order to accommodate measurement over a wider range of wavelength from 790 nm to 900 nm, which is the stable wavelength range that the Ti:Sapphire ultra-fast laser system can operate within. The probe beam is filtered by a short pass filter with cutoff wavelength of 778 nm, when the measurement is carried out at wavelength range beyond 778 nm, the probe beam signal will be cut out by the short pass filter. To solve this, I removed both the short pass filter and the long pass filter for measuring BP optical properties at longer wavelengths. To prevent the pump leaking into the photodetector and interfering with probe beam signal collection, I tuned the mirror before the entrance of the delay stage to offset the pump beam path from the probe beam path. I used an aperture to block the pump beam from entering the photodetector. My measurements results in chapter 4 demonstrated that this geometric separation of pump and probe beams was effective in removing pump beam noise.

In conclusion, the TDTR setup, its data reduction method and the upgraded ps interferometry system are described in this chapter. In the next chapter, the mechanism of Brillouin scattering and ps interferometry data reduction method will be discussed.

Chapter 3 Mechanism of Picosecond Interferometry and Related Data Reduction

3.1 Acoustic Wave Generation

In this section, acoustic wave generation will be discussed. From the previous study on the anisotropic thermal conductivity of BP by Zhu *et al.* [17], the observed V_{in} signal is oscillating in the early time delay of TR-MOKE measurement. This oscillation is caused by Brillouin scattering. Brillouin scattering is the scattering of the light transmitting inside a medium by acoustic waves. In the pump-probe optical technique, the transducer is thermally deformed by the pump heating and launched acoustic waves in to the layers beneath. The acoustic waves travel with corresponding speed of sound in that medium. Upon contact with interfaces, the acoustic wave will be transmitted and reflected [69]. The acoustic wave causes optical interference of the reflected light that contains useful information about the optical and acoustic properties of the sample, which is captured by the V_{in} signal in ps interferometry system. The imaginary part of the signal V_{out}, does not contain information regarding the acoustic wave. Since acoustic wave is a vibrating mechanical wave, the magnitude of acoustic wave will decay as it travels inside the medium. In this section, acoustic wave generation is discussed.

Consider the experimental setup shown in Fig. 2.2(B). The pump and probe beams both at 5 mW power are sent to the surface of metal transducer. Both pump and probe beams are focused by an 10 × objective lens and the resulting beam spot radius is 6 μm. The energy carried by laser beam is given to electrons in metal transducer. Since the diffusivity of heated electron is high, the energy quickly become uniformly distributed in the metal transducer with in ~10^{-13} s [65]. At this timescale, the temperature change ΔT in metal transducer is treated as an impulse function.

For the case which the absorption length δ is less than the metal transducer thickness *d*, the metal transducer is optically opaque and the total energy absorbed by the transducer per unit volume *W(z)* is [67]

$$W(z) = (1-R)\frac{Q}{A\delta}e^{-z/\delta} \tag{3.2}$$

where *R* is the reflectivity of the metal transducer, *Q* is the energy per pulse and *A* is the illumination area (beam spot) . The beam heating causes a temperature rise of $\Delta T = W(z)/C$ where *C* is the metal transducer volumetric specific heat capacity. The isotropic thermal stress in the metal transducer is $-3B\beta\Delta T(z)$ with *B* being the bulk modulus and β being the thermal expansion coefficient. This thermal strain generates an acoustic pulse inside the metal transducer which travels towards the sample substrate.

Whenever the acoustic pulse reaches an interface (*i.e.* the interface between metal transducer and sample substrate), the acoustic pulse will be partially reflected. The fraction of the acoustic pulse reflected at the interface is defined by the reflection coefficient $r_{\mathrm{ac}} = (Z_{\mathrm{s}} - Z_{\mathrm{f}})/(Z_{\mathrm{s}} + Z_{\mathrm{f}})$. The transmitted fraction of the acoustic pulse is defined by the transmission coefficient $t_{\mathrm{ac}} = 2Z_{\mathrm{f}} / (Z_{\mathrm{f}} + Z_{\mathrm{s}})$, where Z_{f} and Z_{s} are the acoustic impedance (defined as $Z = \rho v_{\mathrm{s}}$, the product of material density ρ and the speed of sound v_{s}) of the metal transducer film and the substrate, respectively. Considering the transmission loss of acoustic pulse strength at the metal transducer/sample substrate interface, the amplitude of the first strain η_0 entering the sample substrate is defined as

$$\eta_0 = \frac{1+\nu}{1-\nu}\beta\Delta T \frac{2Z_\mathrm{f}}{Z_\mathrm{f}+Z_\mathrm{s}}\frac{v_\mathrm{f}}{v_\mathrm{s}} \tag{3.3}$$

where ν is the Poisson's ratio of the metal transducer, v_f and v_s are the speed of sound in metal transducer film and sample substrate, respectively. This acoustic pulse represents the longitudinal strain component η_{33} along the through-plane direction [76].The acoustic pulse will continue to travel inside the sample substrate until it incidents onto the sample substrate boundaries and reflects, and its strength is subject to decay due to acoustic damping. The moving acoustic pulse changes the local optical constants *n* and *k* of the sample substrate through the acoustic-optical effect [77]. The change in the optical constants are [67]

$$\Delta n(z,t) = \frac{\partial n}{\partial \eta_{33}}\eta_{33}(z,t) \tag{3.4}$$

$$\Delta k(z,t) = \frac{\partial k}{\partial \eta_{33}}\eta_{33}(z,t) \tag{3.5}$$

In addition to changing the optical properties of the sample substrate, the acoustic wave will also perturb the thermoreflectance signal once it returns to the metal transducer/air interface, a phenomenon known as picosecond acoustic. An example of acoustic wave perturbation on thermoreflectance signal is shown in Fig. 3.1.1. The example considers an acoustic pulse generated inside a 70-nm Aluminum metal transducer traveling towards sample substrate (300-nm SiO_2/bulk Si wafer) at the speed of sound. The picosecond acoustic [78] method is used to determine the thickness of thin film layers in the sample stack. The acoustic pulse that returned to the surface can produce a positive (120 ps in Fig. 3.1.1) or negative (21 ps in Fig. 3.1.1) peak in the thermoreflectance signal. The time delay at which the peaks occur can be used to determine the thickness of each layer. The acoustic pulse is traveling at the speed of sound $v_s = 6.4$ nm/ps in the Al film, reflected from the Al/SiO_2 interface, and returning to the Al/air interface. The round trip would take approximately 21 ps inside the 70-nm Al film. An acoustic pulse round trip between Al/air interface and SiO_2/Si interface would take approximately 120 ps.

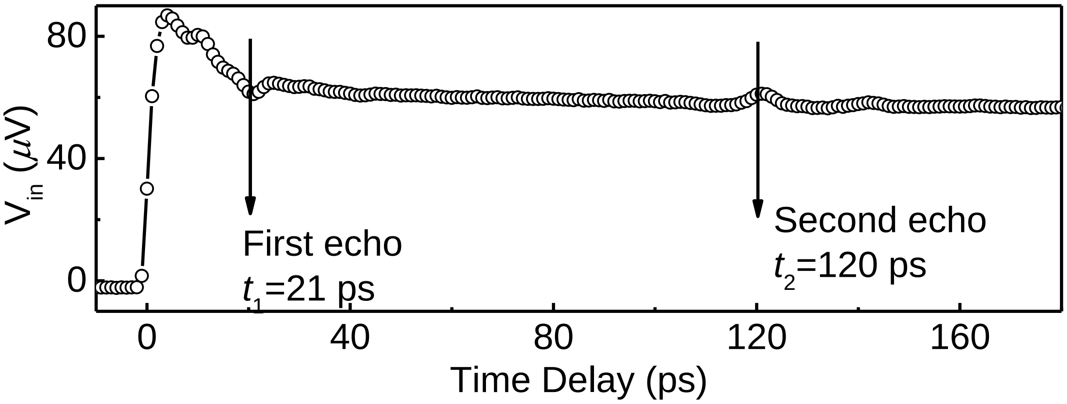

Figure 3.1.1. Picosecond acoustic feature observed from 70-nm Al/ 300-nm SiO_2/bulk Si wafer sample. The arrows at 21 ps and 120 ps indicate the acoustic echo at Al/SiO_2 interface and SiO_2/Si interface, respectively.

The sign of the peaks is determined by the acoustic impedance of the materials on the two sides of the interface. When the acoustic pulse travels from a high acoustic impedance medium to a low acoustic impedance medium, the acoustic pulse will undergo a π phase shift and produce a negative peak in the thermoreflectance signal. If the acoustic pulse travels from a low acoustic impedance medium to a high acoustic impedance medium, the pulse will undergo no phase shift and produce a positive peak in the thermoreflectance signal. In ps interferometry, picosecond acoustic produces similar peaks that are used to estimate the bulk BP thickness. In section 3.2, the detection of acoustic wave in semi-transparent sample stack will be discussed in detail.

3.2 Brillouin Scattering Induced Optical Interference

Brillouin scattering is the scattering of photon due to the nonlinearity in a medium [79], specifically due to the perturbation introduced by acoustic pulses as discussed in the previous section. A schematic diagram of Brillouin scattering in metal transducer/bulk BP is shown in Fig. 3.2.1. When the acoustic pulse caused by the pump heating propagates from the film transducer to the bulk BP, the propagating acoustic wave front becomes a moving Δn grating at velocity v_s. The incoming probe beam is reflected at the metal film surface as primary reflection beam A, and a portion of the probe beam penetrates through the semi-transparent metal transducer. The moving grating will reflect the penetrated probe light back as secondary reflection beam B because the strain changes the local refractive index according to Eqn. (3.5).

Since there is an optical path difference between reflection beam A and reflection beam B, the two reflected beams will optically interfere with each other. This leads to oscillations as a function of time delay in the total reflected probe beam intensity. The magnitude and periodicity of the optical interaction between beam A and beam B is determined by the acoustic and optical properties of the bulk BP flake. By observing the interference pattern, the unknown optical properties of bulk BP at this specified laser wavelength can be extracted [66]. This indirect measurement technique prevents BP degradation from oxidation and water absorption [80]. Applying ps interferometry to an absorbing anisotropic material (*e.g.* BP) is a more complex process compared dealing with non-absorbing isotropic thin film such as SiO_2 or glass [81] . In this study, I developed a polarization-resolved ps interferometry method to probe the anisotropic optical response of bulk BP with thicknesses on the order of a few micron. I developed a bi-exponential decay model to study the optical properties of BP and its birefringent behavior.

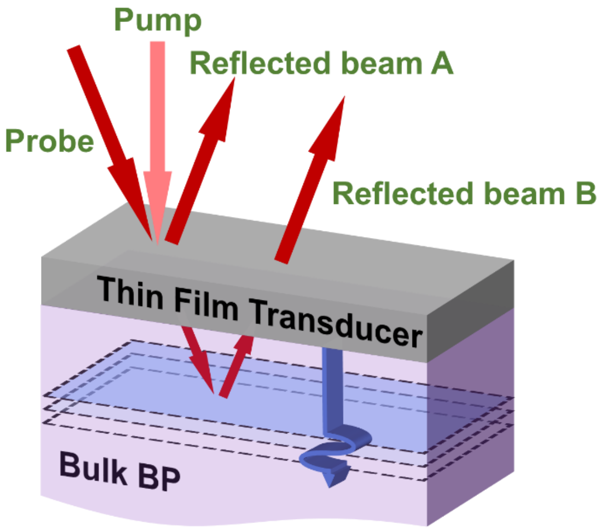

Figure 3.2.1. Schematic diagram demonstrating the Brillouin scattering phenomenon in a front-pump front-probe setup. The pump beam (pink arrow) incident on the thin film transducer, producing an acoustic wave that is propagating downward at the speed of sound in BP (The dash-line blue rectangles indicates the moving acoustic wave front). The probe beam is partially reflected from the transducer surface as beam A and partially penetrated. When the penetrated probe beam incident onto the acoustic wave, which serves as a moving refractive index grating, it gets reflected as beam B.

For non-absorbing isotropic samples, the incident light polarization orientation does not affect the ps interferometry results. The incident electric field of the probe beam is $E_\mathrm{i} = E_0 e^{i(k_0 z - \omega t)}$ where z is the direction of wave propagation, ω is the wave frequency and k_0 is the wave vector in vacuum. The reflected wave at the metal transducer is

$$E_r = r_0 E_0 e^{i(-k_0 z - \omega t)} \tag{3.6}$$

where r_0 is the Fresnel reflection coefficient. Since the acoustic pulse is travelling at the speed of sound on the order of ~5000 m/s inside BP flake, the moving Δn grating is much slower than the speed of light $c = 3\times10^8$ m/s. The local change in refractive index can be treated as quasi-static at any given time delay during the experiment. Such a local variation creates a condition similar to the Bragg condition [82]: instead of photons scattering off atoms in a crystalline system in Bragg condition, the photons scatter at the acoustic wave front. In order to calculate the change in probe reflectivity due to the acoustic pulse inside the BP flake, the Maxwell equations inside the sample substrate need to be solved.

$$\frac{\partial^2 E}{\partial z^2} = -\frac{\omega^2}{c^2}\left[\varepsilon + \Delta\varepsilon(z,t)\right]E(z) \tag{3.6}$$

where ε is the complex dielectric constants inside the BP flake and is related to the optical constants n and κ by $\varepsilon = (n + i\kappa)^2$. $\Delta\varepsilon(z,t)$ is the change in dielectric constants caused by acoustic pulse.

Solving Eqn. (3.6), the Fresnel reflection coefficient at the acoustic pulse r_B is derived to be

$$r_\mathrm{B} = \frac{E_\mathrm{r}}{E_\mathrm{i}} = ik_0 \int \delta n(z,t) e^{-2ikz} dz \tag{3.7}$$

where $\delta n(z,t)$ is the change in the refractive index due to the acoustic pulse as a function of the location of the acoustic wave *z* inside BP at the time delay *t*. The distance *z* can be related to the time delay by $z = v_s t$, the product of the speed of sound in BP and the time delay. The total Fresnel reflection coefficient of the sample stack is then

$$r = r_0 + ik_0 \int \delta n(z,t) e^{-2ikz} dz \equiv r_0 + \Delta r \tag{3.8}$$

The two components of Eqn. (3.8) are the change in reflectivity at the metal transducer caused by pump heating (first term) and the reflection at the acoustic wave front (second term). After integrating Eqn. (3.8) and rearranging, the total change in reflectivity ΔR can be expressed as a function of time delay:

$$\Delta R = |r_0 + \Delta r|^2 \equiv |r_0|^2 + 2|r_0||r_B|\sin(2\pi ft - \phi) \tag{3.8}$$

$$f = \frac{2nv_s \cos(\theta)}{\lambda} \tag{3.9}$$

where the frequency of oscillation f is a function of BP's refractive index (*n*), speed of sound in BP (v_s), the laser wavelength (λ), the phase shift (ϕ) and the laser incident angle (θ), which is normal incident angle in this experiment ($\theta = 0$). The change in reflectivity contains information regarding the temperature decay at the surface of the metal transducer and the oscillation of the reflected light intensity caused by the constructive and destructive interference of reflected probe beam A and B.

So far, the acoustic pulse decay due to acoustic damping has not been considered. Factoring in the acoustic pulse decay to Eqn. (3.8), the ps interferometry signal is governed by the following equation [81]

$$\Delta R = \Delta R_{\mathrm{T}} + S(\lambda)e^{-t/t_{\mathrm{D}}} \sin\left(2\pi ft + \phi\right) \tag{3.10}$$

where ΔR_{T} is the thermoreflectance change, $S(\lambda)$ is the Brillouin scattering coefficient and t_{D} is the decay rate.

When the medium is absorbing like the BP flake, the light attenuation inside the medium must be considered. The light attenuation in BP flake follows Beer-Lambert Law [18] which depends on the optical penetration depth. Equation (3.10) can be generalized to absorbing medium in the following form

$$\Delta R = \Delta R_{\mathrm{T}} + S(\lambda)e^{-t/t_{\mathrm{D}}} \sin\left(2\pi ft + \phi\right)e^{-2\alpha z} \tag{3.11}$$

where $\alpha = 4\pi\eta\kappa$ is the absorption coefficient as a function of wavenumber η. The probe beam travels a distance of 2z inside BP before it starts to interfere with reflected probe beam A, which is reflected by the second exponential decay term $e^{-2\alpha z}$ in Eqn. (3.11).

I found during experiment that the acoustic wave decay is much slower than the light attenuation. I aligned the polarization along the ZZ direction and measured Brillouin scattering for 3600 ps. The Brillouin scattering oscillations are shown in Fig.3.2.2. The launched acoustic wave travels toward the bottom of BP, meanwhile the amplitudes of Brillouin scattering oscillations decreases. The amplitudes of oscillations is the lowest at 670 ps. The decrease in the amplitudes of oscillations is caused by both acoustic wave decay and light attenuation as described in Eqn. (3.11). When the acoustic wave reaches the bottom of BP flake (the interface between BP and the thermal tape), the acoustic wave is reflected at this interface and returns to the top surface. During its return to the top surface, the probe beam travel distance 2z inside BP is decreasing. According to Eqn.

(3.11), this would lead to increased amplitudes of oscillation (see time delay after 670 ps). When the acoustic wave returns to the top surface (1335 ps), the z term in Eqn. (3.11) becomes 0. At this time delay, the amplitude of oscillation represents the acoustic wave decay. I used the amplitude of oscillation at this time delay to estimate the decaying rate t_D. The amplitude of oscillation only decays for 50% at 1335 ps. At 670 ps the amplitude of oscillation decays for 97%. This comparison shows that acoustic decay is much weaker than light attenuation. O'Hara *et al.* and Ma *et al.* also reported that the acoustic wave decay rate is very low in crystalline systems [66, 81]. Therefore the first exponential decay term e^{-t/t_D} is negligible for the model fitting.

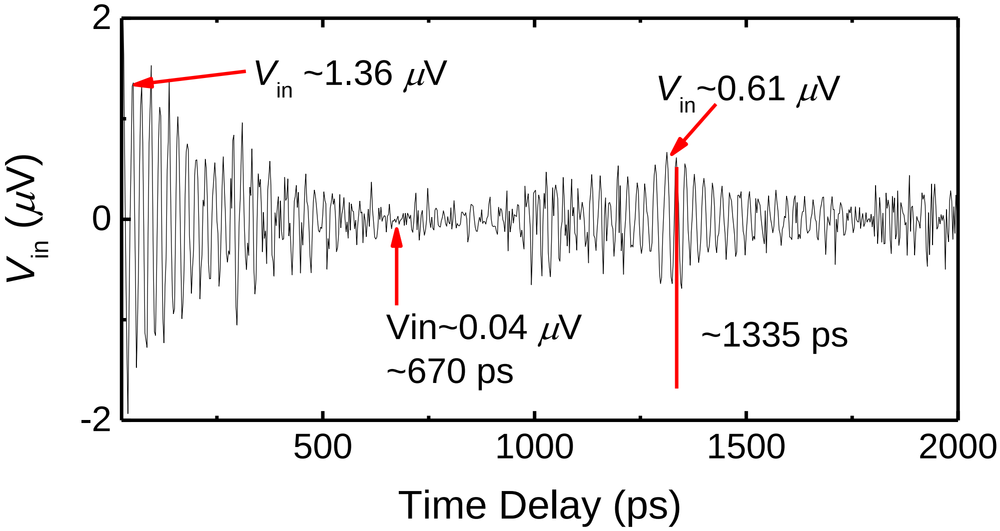

Figure 3.2.2 The ps interferometry measurement on BP. The light polarization is aligned along ZZ direction (least optical absorption direction). The arrow at 1335 ps indicates the time delay at which the acoustic wave return to the top surface.

3.3 Data Analysis for Picosecond Interferometry

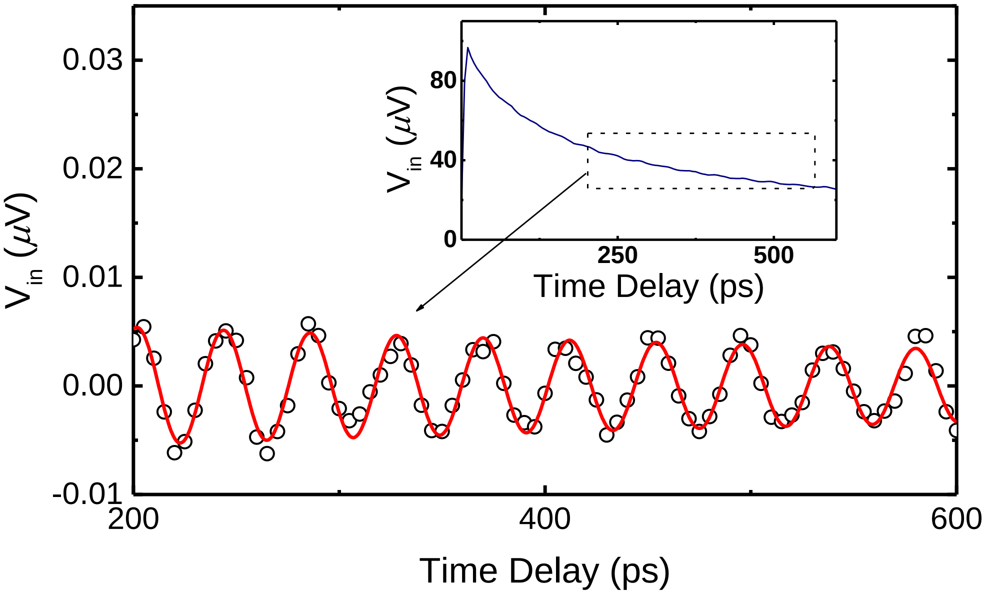

Figure 3.3.1. The ps interference pattern on 5-nm Pt/glass substrate from 200 ps to 600 ps. The thermal background signal is extracted from the data and subtracted to obtain the pure oscillation pattern. The inset plot shows the V_{in} signal in the first 600 ps.

I will present the ps interferometry data analysis for the reference sample of 5-nm Pt transducer/BK7 glass. Based on this data analysis method, the data analysis method for anisotropic absorbing BP flake is discussed. Figure 3.3.1 shows the ps interference pattern measured for the 5-nm Pt transducer/BK7 glass reference sample. The inset of Fig. 3.3.1 shows the original signal without the removal of thermal background. It can be observed from the inset plot that the V_{in} signal is the superposition of typical TDTR thermal decay signal and the oscillating pattern caused by Brillouin scattering. The signal shows a sharp increase in the early ~20 ps time delay, which is caused by the pump heating, and followed by the slow thermal decay as background.

I extracted the thermal background by applying the Savitzky-Golay filter to remove the oscillation pattern. I obtained the ps interference pattern by subtracting the original data with the extracted thermal background. The oscillating pattern is fitted with the following equation:

$$\Delta R(t) = S(\lambda)\sin\left(2\pi ft + \phi\right)e^{-2\alpha z} \tag{3.12}$$

where $S(\lambda)$, f and ϕ are all fitting parameters and $z = v_s t$. The optical absorption coefficient α is set to be 0 because BP-7 glass is non-absorbing. The oscillation pattern has weak amplitudes because the acoustic strain is weak. Typically, for weak Brillouin scattering signal, the signal-to-noise ratio is low, leading to noisier data points (Fig. 3.3.1). For stronger Brillouin scattering oscillations, the signal data will be less noisy as for the BP data shown in chapter 4. The oscillation period is approximately 40 ps. The speed of sound in BK7 calculated from this oscillation period is 6.18 nm/ps, which is close to the speed of sound in fused silicate within a 3% error. The fitting result confirmed that the ps interferometry system is reliable.

At an arbitrary polarization angle between zigzag and armchair directions, Eqn. (3.12) is not sufficient in describing the birefringent behavior of BP, and the combined absorption of κ_{ZZ} and κ_{AM} must be considered. For linearly polarized light oriented at an arbitrary angle θ_{p}, t the intensity of the reflected wave is $S = |E|^2 / 2\eta_0$ where η_0 is the free space impedance and E is the electric field as a function of the incident polarization angle. The reflected electric field can be decomposed into two polarization components as $E_r = e_x E_x + e_y E_y = |E_r|\left(e_x \cos\theta_{\mathrm{p}} + e_y \sin\theta_{\mathrm{p}}\right)$.The sum of x and y direction intensity components is $S = \left(|E_{rx}|^2 + |E_{ry}|^2 \right) / 2\eta_0$. In this case, the change in reflectivity at an arbitrary polarization angle θ_p is

$$\Delta R(\theta_\mathrm{p}) = \Delta R(\mathrm{ZZ}) \cos^2 \theta_\mathrm{p} + \Delta R(\mathrm{AM}) \sin^2 \theta_\mathrm{p} \tag{3.13}$$

Experiment data at any angle between ZZ and AM directions can be fitted by substituting the polarization angle, κ_ZZ and κ_AM into the bi-exponential decaying model

$$\begin{gathered} \Delta R(\theta_\mathrm{p}) = S(\lambda)[\cos^2 \theta_\mathrm{p} \exp(-2\alpha_\mathrm{ZZ} v_\mathrm{s} t) \cos(\frac{2\pi n v_\mathrm{s} t}{\lambda} - \phi_\mathrm{ZZ}) \\ + \sin^2 \theta_\mathrm{p} \exp(-2\alpha_\mathrm{AM} v_\mathrm{s} t) \cos(\frac{2\pi n v_\mathrm{s} t}{\lambda} - \phi_\mathrm{AM})] \end{gathered} \tag{3.14}$$

Based on Eqn. (3.13), the amplitudes of oscillations should also follow the bi-exponential decaying trend to properly describe the birefringent behavior of BP. This is demonstrated by the excellent agreement between the measurement and the model calculation in chapter 4:

$$A(\theta_\mathrm{p}) = \cos^2 \theta_\mathrm{p} \exp(-2\alpha_\mathrm{ZZ} v_\mathrm{s} t) + \sin^2 \theta_\mathrm{p} \exp(-2\alpha_\mathrm{AM} v_\mathrm{s} t) \tag{3.15}$$

Chapter 4 Picosecond Interferometry Study on Black Phosphorus: Results and Discussion

4.1 Controlled Experiments

I performed ps interferometry experiments at 783 nm on three samples: 20-nm TbFe/BP, 5-nm Pt/BP, and the bare bulk BP. Since BP is known for oxidation degradation, in order to shorten the amount of time that the BP is exposed to oxidation environment, the pure bulk BP sample was prepared by peeling off the Pt film on the Pt/BP sample just before the experiment. The Pt layer was peeled off from the bulk BP by adhering a piece of Scotch tape to the sample Pt surface and then tearing off the Scotch tape to remove the Pt film as well as the top few layers of BP. The same sample were measured several times to ensure that the results are repeatable and reliable. I further conducted ps interferometry measurements at 835 nm and 890 nm on the 5-nm Pt/BP sample and analyzed the oscillation frequency and its decaying rate to extract BP's anisotropic optical properties.

For the 20-nm TbFe/BP measurements, I measured 7 incident light polarization angles (θ_p) in between 0^o and 90^o. The laser polarization direction was held stationary while the sample was rotated. The ZZ and AM directions were determined from the in-plane thermal conductivities measurements performed by Zhu *et al.* in the MNTTL group [17]. Since BP is known for its anisotropic thermal conductivities along the ZZ, AM, and through-plane directions, a 2D FWHM [83] contour scan of the BP can accurately determine the ZZ and AM crystalline directions. At each θ_p, the Brillouin scattering pattern was measured from 0 ps to 1000 ps time delay, since at longer time delays the Brillouin signal became significantly noisier and therefore contained very little useful information. The Brillouin scattering pattern at each θ_p was normalized by the magnitude of its first peak, such that we only compare the relative amplitude of oscillation at different θ_p. I also examined the normalized thermal background.

The 5-nm Pt/bulk BP sample was prepared in addition to the TbFe/BP sample to verify the measurement results obtained from the TbFe/BP sample. The 5-nm Pt/bulk BP sample has an advantage over the TbFe/bulk BP sample resulting from its much thinner transducer compared with that of the TbFe/bulk BP sample. The Pt transducer absorbs less laser energy, therefore the reflected beam B (see Fig. 3.2.1) intensity would be stronger. This will enhance the optical interference effect and increase the amplitude of Brillouin scattering, which improves the signal-to-noise ratio and measurement accuracy.

4.2 Results and Discussions

The normalized ps interferometry measurement data from TbFe/BP sample are shown in Fig. 4.2.1(A) and its normalized thermal background is shown in Fig. 4.2.1(B). Figure 4.2.1(A) demonstrated the increasing oscillation decay rate from ZZ polarization direction to AM polarization direction. Figure 4.2.1(B) shows that the thermal background in this sample measurement is different from the typical thermal background observed from TDTR measurement as shown in Fig. 2.3.2(A). The thermal background of TbFe/BP does not exhibit a monotonic decaying trend. The first peak caused by pump excitation is at 50 ps, and there is a second broader peak at approximately 300 ps. The cause of the second peak is analyzed and will be discussed in the next section.

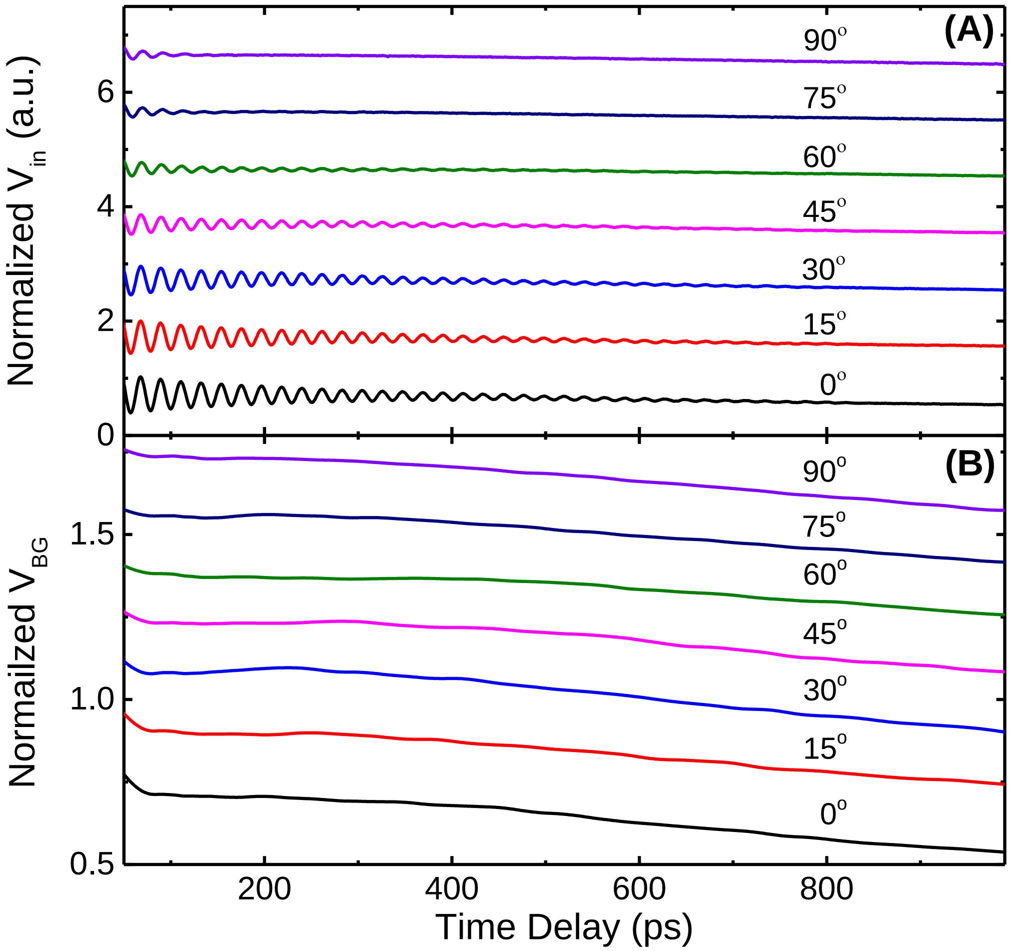

Figure 4.2.1 The measurement results of TbFe/BP sample. (A) The normalized original signal at various polarization angles (θ_p). (B) The thermal background signal V_{BG} obtained by applying the Savitzky-Golay smoothing filter to the original data to smooth out the oscillation.

The pure oscillation signal is separated from the original signal by subtracting the extracted thermal background as shown in Figs. 4.2.2(A) and (B). The oscillation signals at ZZ and AM are fitted with Eqn. (3.12). The fitting gives absorption coefficients κ_{ZZ}

and κ_{AM} of 0.031 and 0.204 respectively, which are comparable to literature values of 0.017 and 0.210 reported by Schuster *et. al* [25]. The difference between my measurement values and the literature values is contributed to the difference in measurement condition. They measured bulk BP flake at T = 20 K, and their BP sample thickness was 100-200 nm. Because BP properties can vary with temperature and number of layer [10, 12], my measurement results deviate from their reported results by approximately 10~30%. The phase shift term ϕ obtained from fitting is ~0.5 for all polarization angles. Because Brillouin scattering measures the reflected light from inside of a crystalline system, the phase shift is related with the refractive index n of the crystalline system. The consistency of phase shift term ϕ at all polarization angles implies that n is weakly dependent on θ_p.

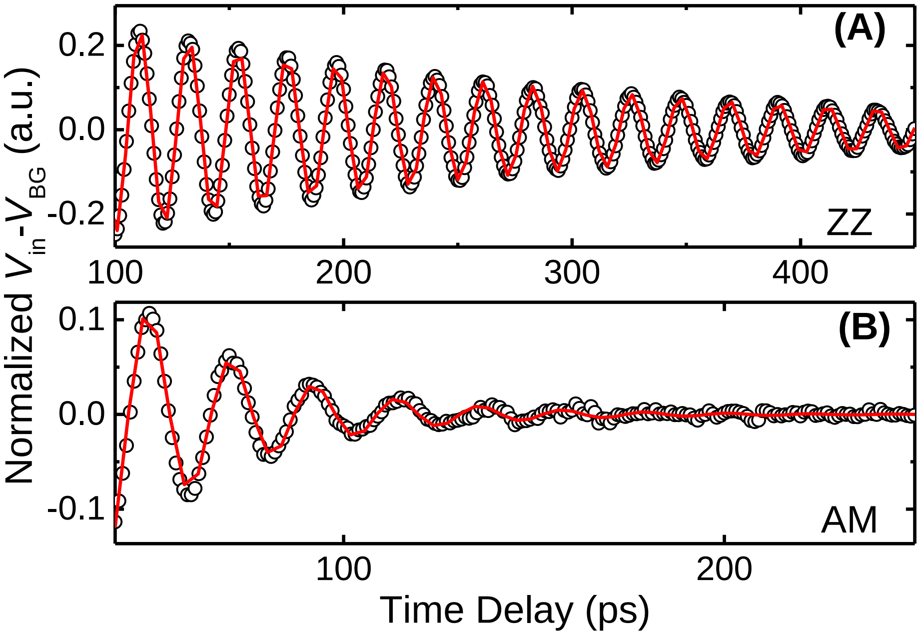

Figure 4.2.2 (A) and (B) are the pure oscillation signal along the ZZ (least absorbing, $\theta_p = 0^o$) and AM (most absorbing, $\theta_p = 90^o$) directions, respectively. The open circles are original data and the red solid lines are the fitting of the signal based on Eqn. (3.12).

The fitting also extracts the period of oscillation (~21 ps) and the corresponding frequency of oscillation ($\sim 46 \pm 1$GHz) for incident light polarized at all polarization angles. This is confirmed by applying Fast-Fourier Transform (FFT) to the original signals as shown in Fig. 4.2.3, which reveals that the frequency of oscillation ranges from 46.2-47.3 GHz. The magnitudes of the full width at half maximum (FWHM) of the FFT peaks are related to the amount of light absorbed at each θ_p. Since the light absorption is the smallest along the ZZ direction [12, 13, 45], the Brillouin scattering pattern lasts longer than 900 ps time delay and the oscillation decay rate is the smallest. This results in a high signal-to-noise ratio. Correspondingly, the FFT peak at 46.2 GHz for the ZZ direction has a very narrow FWHM and the highest peak intensity.

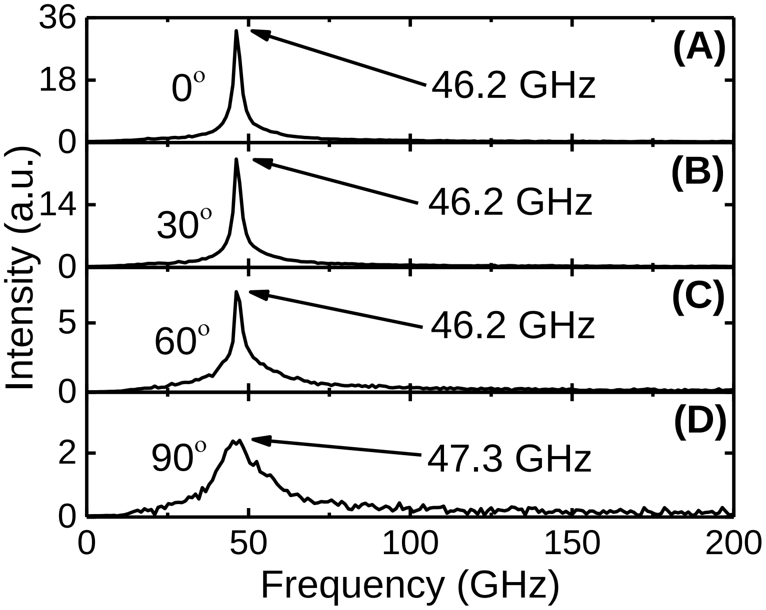

Figure 4.2.3 The FFT analysis of the original ps interferometry signal at difference polarization angles: (A) θ_p = 0°, (B) θ_p = 30°, (C) θ_p = 60°, and (D) θ_p = 90°. These frequency is substituted into Eqn. (3.9) to extract the real part of refractive index *n* of bulk BP.

As θ_p rotates from ZZ towards AM, the FFT peak magnitude gradually decreases due to the increase of light absorption. The intensity of the FFT peak is the smallest and the FWHM of the FFT peak is the widest along AM. Figure 4.2.3(D) shows that there is a series of smaller FFT peaks between 50 GHz and 200 GHz and below 40 GHz. Since the Brillouin scattering oscillation quickly vanishes within 200 ps time delay for the AM orientation, there is not observable Brillouin scattering oscillation after 200 ps and the signal-to-noise ratio becomes smaller. Therefore, more noise is observed in the FFT analysis. The lower signal-to-noise ratio also contributes to the broadening of the peak FWHM for the AM orientation.

Using the longitudinal speed of sound of bulk BP (4.76 nm/ps) [84], the real part of dielectric constants n can be calculated using Eqn. (3.9) assuming the angle of incidence is normal to the sample surface. The measured n values range from 3.78 to 3.86. This is an evidence that the refractive index (n) of bulk BP along the through-plane direction is isotropic regardless of the in-plane crystalline direction. Note that the angle of incidence can be slightly misaligned from the normal angle of incidence, possibly resulting from the imperfect horizontal sample loading during the mechanical exfoliation process. However, a 5-degree deviation from the normal incidence will induce approximately only 4% error to the n value, based on Eqn. (3.9). Since the n values obtained from the experiment at different angles are fairly consistent and close to the literature value of 3.83 [25] measured from the EELS measurement, the uncertainty caused by the angle of incidence should only induce negligible errors to the measurement results.

For the Pt/BP sample, the ZZ and AM crystalline directions were determined from the ps interferometry measurements. One approach of determining crystalline direction is to look at the amplitude of the thermal background. For θ_p along ZZ direction, the BP absorbs the least amount of light and generates the least amount of heat. This leads to the smallest thermal background, which is the sum of heat generated within the Pt transducer and BP. For θ_p along AM direction, the BP absorbs the highest amount of energy and generates the largest amount of heat, and therefore leads to the largest thermal background. During experimental observation, this approach serves as a good reference for a rough estimation of the crystalline direction. However, the thermal background data taken within 10^o near the AM or ZZ direction have very similar magnitudes. Thus, the accurate ZZ and AM directions cannot be determined by this method.

A more accurate method to determine the ZZ and AM directions in 5-nm Pt/BP sample is to perform incremental scan of ps interferometry measurements at various polarization angles and use Eqn. (3.12) to fit for an exponential decay constant. The exponential decay constants at ZZ and AM directions should be the lowest and highest, respectively, therefore allowing very accurate identification of ZZ and AM crystalline directions within $\pm 2^\circ$ accuracy. To find the ZZ and AM directions, the incremental scan must cover at least 90^o range. During this study, 110^o range scans were performed to ensure that both ZZ and AM crystalline directions can be captured.

After the ZZ and AM crystalline directions are determined by fitting the measurement data with Eqn. (3.12), the thermal background was extracted. I fit the Brillouin scattering signals obtained at varying θ_p between ZZ and AM directions with

Eqn. (3.14). The thermal background of Pt/BP sample is shown in Fig. 4.2.4(A). It is discovered that the excitation process is very slow at early time delay. The thermoreflectance signals at early time delay (~80 ps) is negative. This is contributed to the thermoreflectance signal from BP. Detailed analysis on the complicated thermoreflectance signal before 700 ps will be provided in the next section.

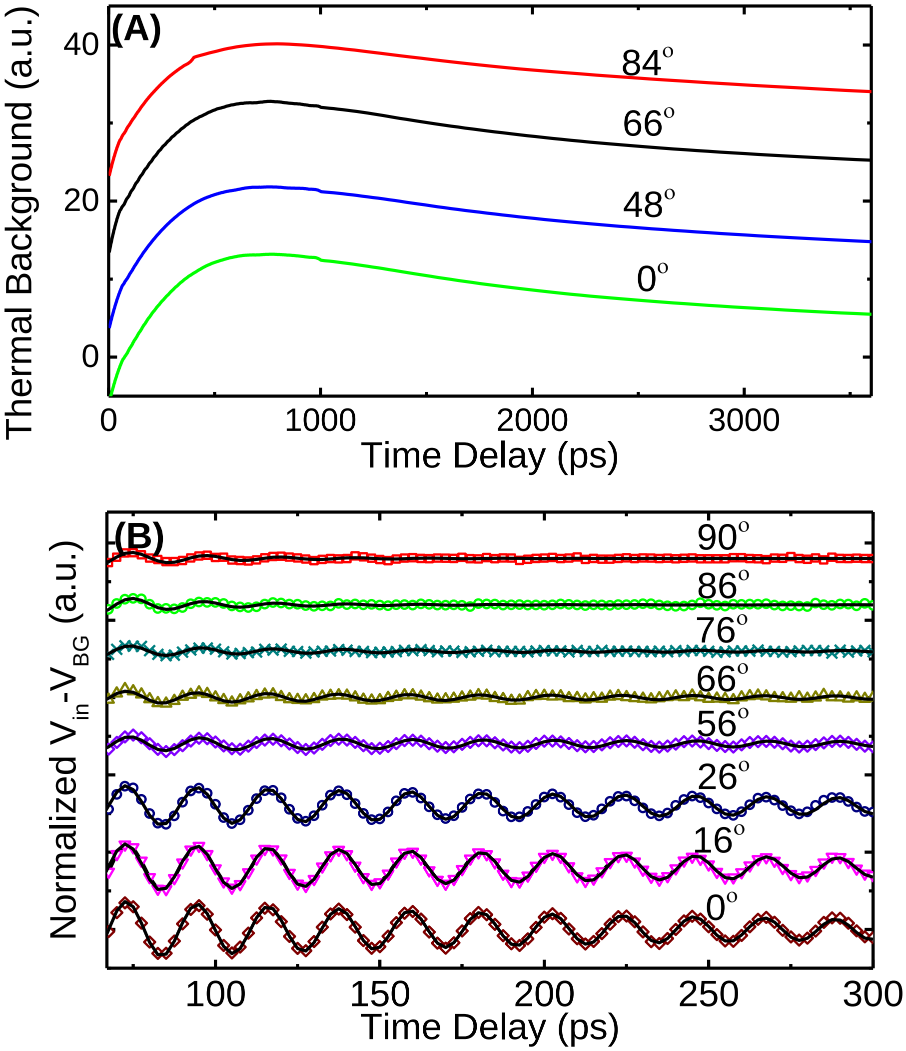

Figure 4.2.4 (A) The thermal background obtained by applying the Savitzky-Golay smoothing filter to original ps interferometry signals. The thermal backgrounds are offset from each other for better visualization. (B) The original ps interferometry signals at various θ_p between 0° and 90° (symbols) and the model fitting result (solid lines).

Figure 4.2.4(B) shows the oscillations isolated from the thermal background and the associated fitting results. The amplitude of oscillation is the highest at ZZ and the lowest at AM. The oscillation decay is the fastest at AM and the slowest at ZZ. These observations indicate that BP has strong anisotropic optical absorption. The extracted n value is 3.77 and the k_{ZZ} and k_{AC} values are 0.040 and 0.210, respectively.

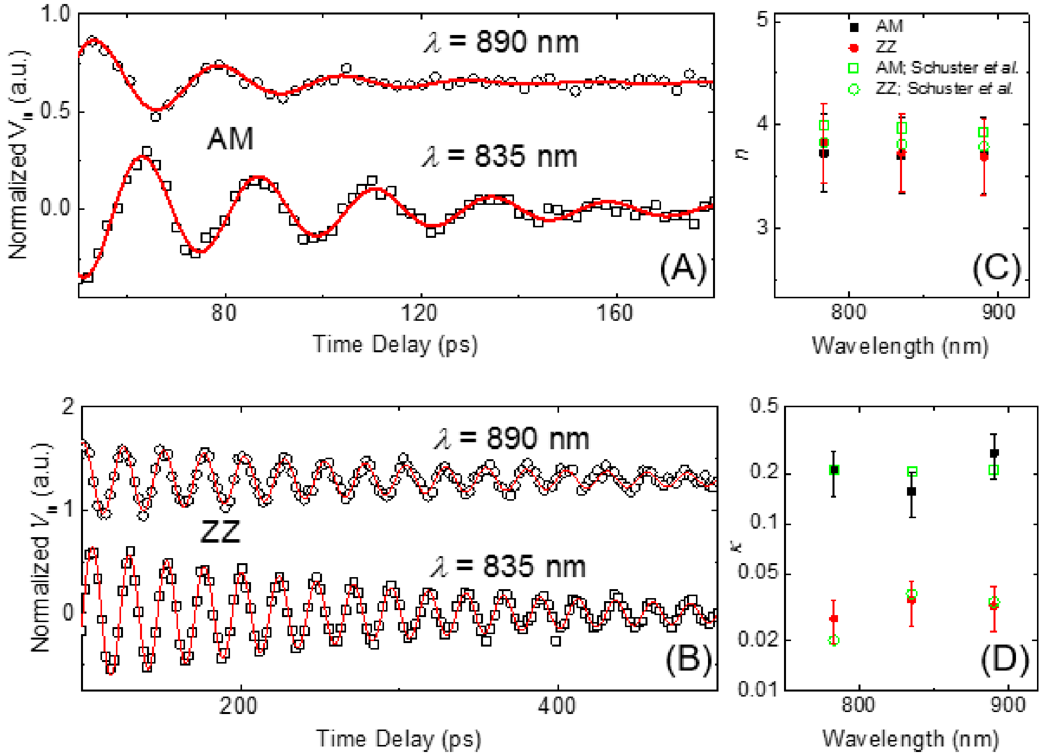

Figure 4.2.5 Picosecond interferometry measurements at 835 nm and 890 nm; (A) and (B) are the oscillation signals (symbols) along AM and ZZ directions, obtained at 835 nm and 890 nm. The fitting results based on Eqn. (3.12) are shown as red solid lines. (C) Extracted n values. Black solid squares are the measured values along the AM direction and the solid red circles are the measured values along the ZZ direction. The error bars are 10%. (D) Extracted k values. Black solid squares are the measured values along the AM direction and the solid red circles are the measured values along the ZZ direction. Green open symbols in (C) and (D) are literature values from EELS measurements [25].The error bars are 30%.

The Pt film was peeled off by Scotch tape and the bare BP was measured again at 783 nm. The same optical properties were obtained for bare BP, which shows that the experiment is repeatable and the measured optical properties are reliable. The experiments were repeated at 835 nm and 890 nm as shown in Figs. 4.2.5 (A) and (B). The measurement results of optical properties of BP at all three wavelengths are summarized in Figs. 4.2.5 (C) and (D).

To verify that the decay of oscillation signal follows the bi-exponential decaying trend, the peak amplitudes of oscillations as a function of time delay are extracted and compared with the calculated results based on Eqn. (3.15). Figure 4.2.6 demonstrates that the amplitude of oscillation agrees well with the calculation result of Eqn. (3.15). This justifies that the light absorption of BP contains two components, and each has its contributions from either ZZ or AM optical absorption.

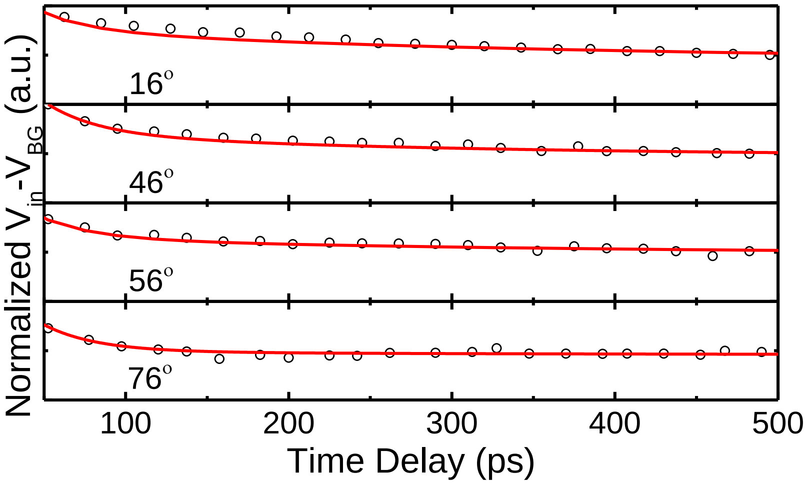

Figure 4.2.6 The peak amplitudes of oscillations at 4 different polarization angles plotted as a function of time delay. Calculation based on Eqn. (3.13) is also shown as red solid lines for comparison.

To better illustrate the effectiveness of the optical property measurement through ps interferometry, I conducted the sensitivity calculations of the measurement signals to different parameters. Whenever a small change is introduced to a measurement parameter x (absorption coefficient κ, frequency f and phase shift ϕ), the system responses with a sensitivity $S(x)$. The sensitivity is defined as $S(x)=\frac{\partial(-V_{\mathrm{in}})/\max(V_{\mathrm{in}})}{\partial x/x}$ where $\max(V_{\mathrm{in}})$ is the amplitude of the first oscillation.

In the sensitivity calculations, a small perturbation 0.2% is introduced as ∂x. The system response to the introduced error is calculated and plotted as time delay dependent sensitivities shown in Figs. 4.2.7(A) and (B). It is revealed that the sensitivity is also oscillating in nature, and the measurement is most sensitive to frequency f, which corresponds to the refractive index n, and is least sensitive to the absorption coefficient κ. For ZZ direction, the sensitivity is large enough throughout the first 1000 ps time delay to measure precise and reliable κ value. However, for AM direction, the sensitivity to k quickly vanishes within the first 200 ps time delay, therefore results in measurement data with higher uncertainty.

The measurement is also fairly sensitive to the phase shift ϕ, but its sensitivity depletes as time delay increases because of light attenuation inside BP. This is trivial when Fig. 4.2.7(A) and (B) are compared, in which measurement along AM crystalline direction quickly loses sensitivity. The duration of time delay with reasonable sensitivity also determines what thickness of the sample is required to gather data via picosecond interferometry. For example, in the case of BP the sensitivity along AM direction is significant for the first 200 ps, which means that it requires only 1.6 μm thick BP to gather useful data along the AM crystalline direction. Sensitivity analysis can help better design ps interferometry measurement for 2D materials.

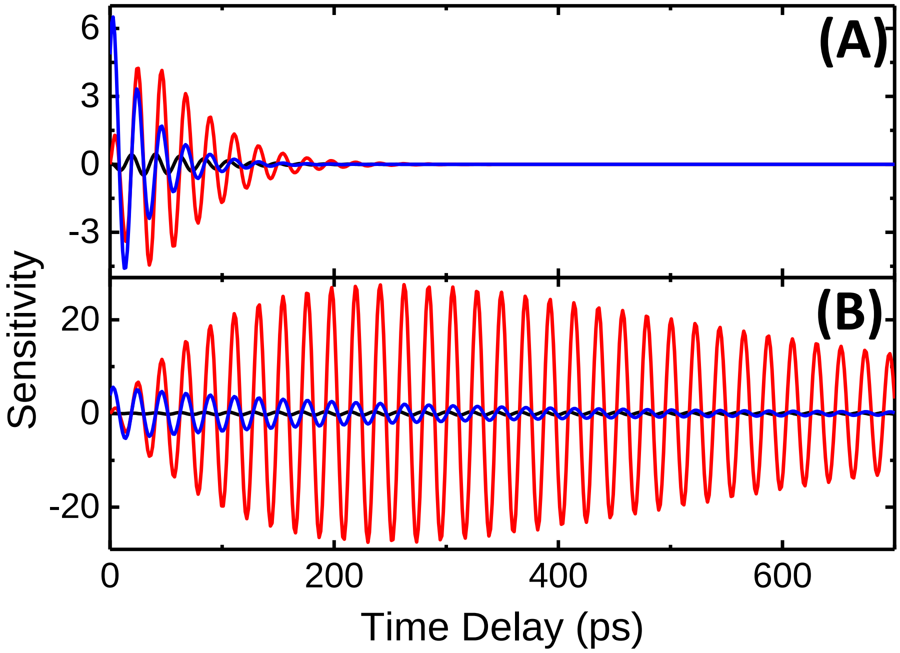

Figure 4.2.7 The sensitivity calculation plots for both (A) ZZ, and (B) AM crystalline directions of BP. The black line is the sensitivity to optical absorption coefficient κ, the red line is that to frequency f, and the blue line is that to phase shift ϕ .

4.3 Electromagnetic and Thermal Simulation

To better understand the behavior of thermal background, I used FDTD and ANSYS CFX to conduct electromagnetic simulation and thermal simulation, respectively, to analyze heat flow in the sample stack. The thermal background of typical TDTR measurements exhibits monotonic decaying trend after the initial excitation process at the very early time delay (less than 10 ps), as shown in Fig. 2.3.2(A). However, the thermal background V_{BG} of my BP samples shows either very slow excitation process on the order of several hundreds of ps (see Fig. 4.2.4 (B)) or an increase in V_{BG} during the first 300 ps after the initial excitation (see Fig. 4.2.1(B)). For bare BP measurements, the temperature rise due to the initial excitation is slow and the monotonic temperature decay starts after ~300 ps as shown in Fig. 4.3.1.

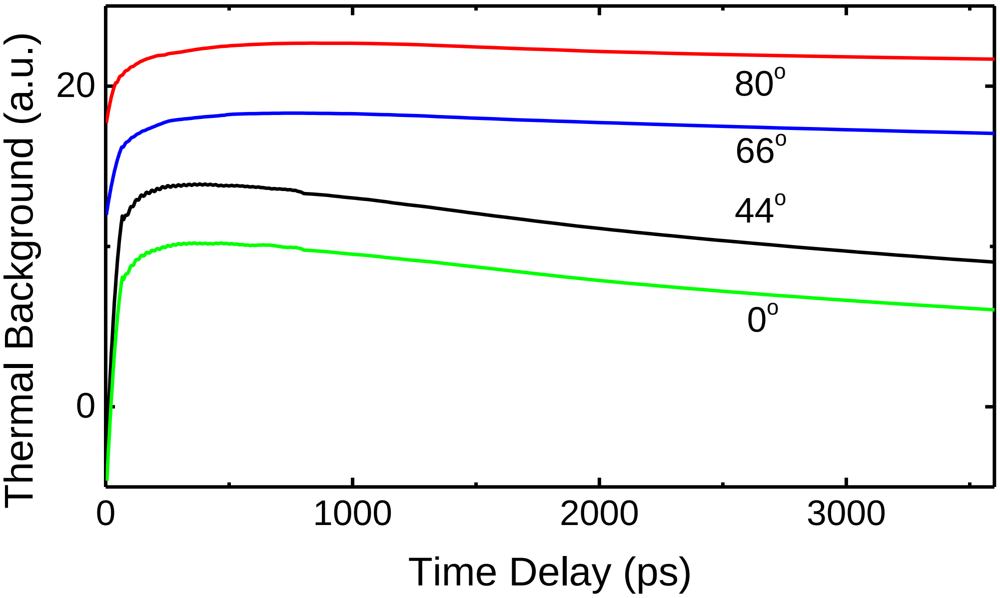

Figure 4.3.1 The thermal background obtained from bare BP measurements at varying θ_p. The data are plotted after applying the Savitzky-Golay smoothing filter to the original Brillouin scattering oscillation pattern.

Firstly, the origin of this unusual thermal background is speculated as the internal heat generation inside bulk BP. Since bulk BP is absorbing heat in ps interferometry measurement, it is possible that the heat generated inside BP is transferred back to the transducer. The heat backflow can raise the temperature at the transducer and cause the increase in V_{in} after the initial excitation. To test this hypothesis, I performed electromagnetic and thermal simulations to mimic the heat generation and heat propagation processes inside a 20-nm TbFe/bulk BP sample. The temperature change at the transducer surface is monitored in the transient thermal simulation with ANSYS. If the simulation shows that the transducer surface temperature has raised after the pump excitation, the thermoreflectance signal should also increase correspondingly; therefore, it would suggest that the hypothesis is true.

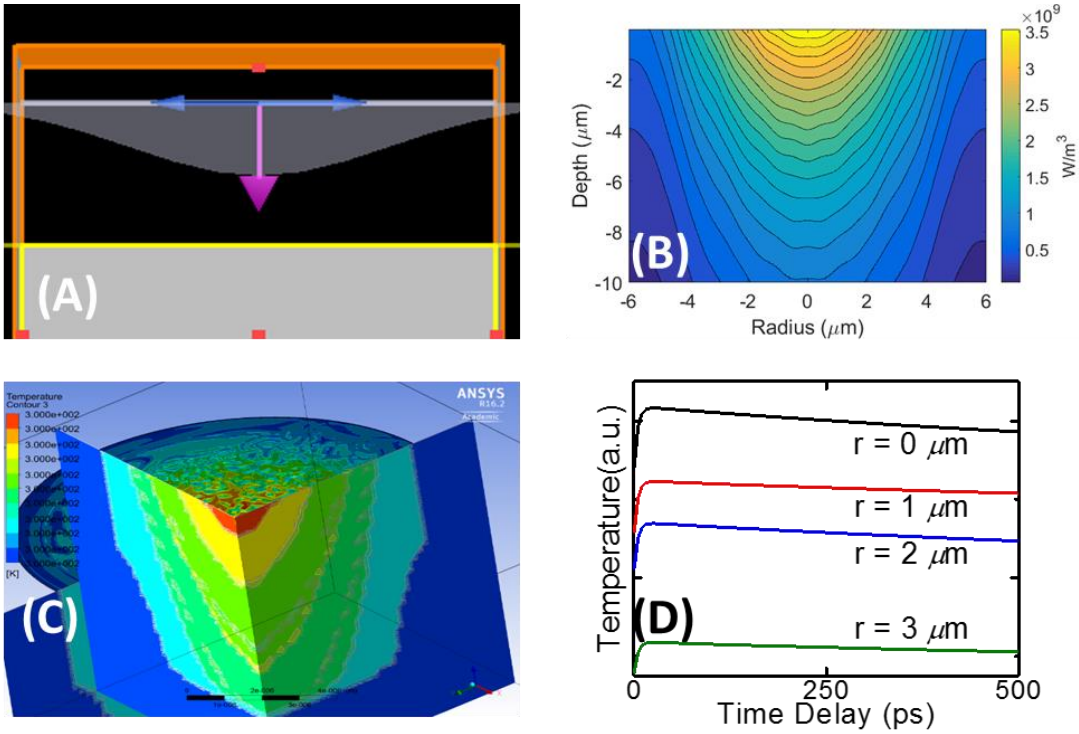

Figure 4.3.2 (A) The cross-section view setup for FDTD simulations. The Gaussian profile indicates a light source consisting of a Gaussian beam traveling toward the 20-nm TbFe/bulk BP. (B) The energy distribution inside BP calculated with FDTD. (C) The temperature distribution inside BP with the ANSYS simulation. The circular temperature contour on top indicates the TbFe surface covered by beam spot area. The cross sections show the temperature contour inside BP. (D) The temperature evolution on the TbFe surface at various radii from the center of the illumination area.

The heat generation process is modelled with a combination of FDTD Solutions and ANSYS. To model the laser absorption, a Gaussian beam with a radius of 6 μm and pulse duration of 1 ps is sent to a 20-nm TbFe/BP sample stack in FDTD. The cross-section view of the FDTD simulation setup is shown in Figs. 4.3.2(A) and (B), where the top and bottom boundaries are set as perfectly matching layer (PML), and the left and right boundaries are set to be periodic. The FDTD simulation is set to be axial-symmetric and two-dimensional to save computational time. Since the optical properties of TbFe is unknown, I approximate its optical properties as those of Fe. The optical properties of BP measured at 783 nm is fed into this simulation. The energy absorption and energy distribution after 1 ps in BP are calculated with FDTD.

The output of the energy distribution simulation is an array of matrix which can be imported into ANSYS CFX simulation tool. The 2D matrix is rotated 360^o with respect to the center axis of the laser beam to form a 3D axial-symmetric conic energy distribution profile in ANSYS CFX, as shown in Fig. 4.3.2(C). The energy distribution profile serves as the initial condition in ANSYS CFX. The initial energy is fed to the simulation structure for 1 ps, simulating the 1 ps heating process. After 1 ps, a transient thermal simulation is set to run for 1 ns in ANSYS CFX and the temperature of the transducer surface is monitored throughout the simulation time duration. The temperature profile of the TbFe transducer along the beam radius *r* is depicted in Fig. 4.3.2(D), which shows a slow excitation process of ~30 ps followed by monotonic temperature decay.

This simulation suggests that there is not heat backflow from BP to the TbFe surface; therefore, thermal propagation is most likely not the cause of the non-monotonic thermoreflectance signal decay. The FDTD simulation and analytical method based on the transfer-matrix approach [75] indicate that there are about 22% of light penetrates through the 20-nm TbFe layer. This means that the thermoreflectance signal directly from BP might have contributed to the overall thermal background. Since BP is a semiconductor and its thermoreflectance coefficient can be non-linear [85], it can change the shape of the overall thermal background. The detail mechanisms that cause the slow excitation process and non-linear thermoreflectance coefficient of BP would require future studies on BP.

Chapter 5 Summary and Outlook

5.1 Summary

Black Phosphorus is an emerging 2D material with great potentials in electro-optical thermoelectric applications [11, 21, 46, 48, 86]. The tunable bandgap, anisotropic transport and optical properties of BP make it an attractive material candidate for future nanoscale device. It has been applied to optical devices such as polarization-sensitive photodetector and field-effect transistors; however its optical properties have not been extensively investigated experimentally. In my master study, I used a modified ps interferometry method to investigate the anisotropic optical properties of BP.

Experimentally, the all-optical pump-probe ultrafast laser technique based on TDTR setup is described in chapter 2. This measurement system, originally developed to investigate the thermal transport properties of thin-film materials *via* thermoreflectance [71, 87, 88]. I upgraded it into ps interferometry [66] to measure the optical properties of BP. In addition, the ability to change polarization has been added to the experimental setup in order to investigate the birefringent optical response of BP. The sample synthesis and preparation processes are also presented in chapter 2. BP is known for degradation due to oxidation when exposed to ambient environment [80]. Therefore, the BP flake used in this experiment was coated with various metal transducers similar to the approach in previous study [17] *via* sputtering to isolate BP from the ambient environment.

I discussed the acoustic wave generation, propagation, and detection in chapter 3. Unlike the previous ps interferometry methods performed by others [65, 67, 68, 81], I used ps interferometry to study the light attenuation inside BP. This approach indirectly measures the optical properties of BP without exposing the sample to ambient environment, whereas the conventional optical spectroscopy measurements [64]cannot. It can also extract the optical properties without knowing the exact sample thickness of BP and the optical transmission through BP, therefore it simplifies the data reduction. I developed a thermal background removal procedure and bi-exponential fitting model to study the birefringent optical response of BP.

Finally, I discussed the optical properties of BP and its thermal background in chapter 4. The Brillouin scattering oscillation patterns measured from BP are studied at three wavelengths between 780 nm and 900 nm. The measurements with different metal transducers on BP or bare BP produce repeatable results, indicating that the measurement results are accurate and reliable. I fitted the measurement data with an exponentially decaying function to extract optical properties along the ZZ and AM crystalline directions. The optical responses for linear polarized light aligned between ZZ and AM directions were modelled by a bi-exponential decay function. The refractive index n is largely independent of incident light polarization angle and the absorption coefficient κ exhibits a strong dependence on the polarization angle. The largest (least) absorption was obtained when the light polarization was aligned along the AM (ZZ) direction. I also investigated the thermal background of the samples computationally. I discovered that BP's non-linear thermoreflectance coefficient reshapes the thermal background of the measurements. The detail mechanism that causes BP's non-linear thermoreflectance coefficient requires further study.

5.2 Outlook and Conclusion

In this thesis, the all-optical pump-probe ps interferometry was used to study the birefringent optical response of bulk BP to provide valuable data for the fabrication of future BP-based nano-devices. This study demonstrates that the ps interferometry technique holds great potentials in characterizing the optical and mechanical properties of BP and other 2D materials. Due to the limitation of our laser system, only the optical properties between wavelength of 780 nm and 900 nm were measured during this study. However, BP has demonstrated good responsivity in nanophotonic devices over the spectrum range from 350 nm to 1000 nm [48]. The optical properties of the BP over a wider range of electromagnetic spectrum can be measured if the ultrafast laser system is improved to generate ultra-broadband pulses similar to that of Manzoni *et al.* [89]. Based on the study of Antonelli *et al.*[90], the decay rate of acoustic wave in optically absorbing sample substrate may be characterized if the acoustic reflection coefficients at the sample substrate boundaries are known [67]. The transverse speed of sound and the in-plane real part of dielectric constant *n* of BP can also be characterized if the sample is specifically designed to generate transverse acoustic wave as described in the study by Matsuda *et al* [76]. This would be beneficial for understanding the anisotropic in-plane speed of sound and the estimation of lattice thermal conductivity [91]. Furthermore, ps interferometry can be used to investigate BP's coupling effect with strain [14, 22] when an in-plane stress is applied on BP thin film, the BP's electrical and optical properties can be tuned to achieve desirable functionalities. Utilizing ps interferometry with compatible temperature control chambers provides a mean to investigate the temperature-dependent properties of materials [12]. Lastly, the thermoreflectance coefficient of BP, which is non-linear in short time delay as described in chapter 4, implies that there is a complex mechanism that causes BP to behave anomalously under photon excitation. This mechanism requires further study to better understand the thermal background behavior observed in this study.

REFERENCES

1. Bridgman, P., Journal of the American Chemical Society, 1914. **36**(7): pp. 1344-1363
2. Keyes, R.W., Physical Review, 1953. **92**(3): pp. 580
3. Berger, C., Song, Z., Li, T., Li, X., Ogbazghi, A.Y., Feng, R., Dai, Z., Marchenkov, A.N., Conrad, E.H. and First, P.N., The Journal of Physical Chemistry B, 2004. **108**(52): pp. 19912-19916
4. Eda, G., Fanchini, G. and Chhowalla, M., Nature nanotechnology, 2008. **3**(5): pp. 270-274
5. Novoselov, K.S., Geim, A.K., Morozov, S.V., Jiang, D., Zhang, Y., Dubonos, S.V., Grigorieva, I.V. and Firsov, A.A., science, 2004. **306**(5696): pp. 666-669
6. Liu, H., Du, Y., Deng, Y. and Peide, D.Y., Chemical Society Reviews, 2015. **44**(9): pp. 2732-2743
7. Brent, J.R., Savjani, N., Lewis, E.A., Haigh, S.J., Lewis, D.J. and O'Brien, P., Chemical Communications, 2014. **50**(87): pp. 13338-13341
8. Yasaei, P., Kumar, B., Foroozan, T., Wang, C., Asadi, M., Tuschel, D., Indacochea, J.E., Klie, R.F. and Salehi ‐ Khojin, A., Advanced Materials, 2015. **27**(11): pp. 1887-1892
9. Kang, J., Wood, J.D., Wells, S.A., Lee, J.-H., Liu, X., Chen, K.-S. and Hersam, M.C., ACS nano, 2015. **9**(4): pp. 3596-3604
10. Tran, V., Soklaski, R., Liang, Y. and Yang, L., Physical Review B, 2014. **89**(23): p.235319
11. Zhang, R., Zhang, Y., Yu, H., Zhang, H., Yang, R., Yang, B., Liu, Z. and Wang, J., Advanced Optical Materials, 2015. **3**(12): pp. 1787-1792
12. Xia, F., Wang, H. and Jia, Y., Nature communications, 2014. **5**: p.4458
13. Qiao, J., Kong, X., Hu, Z.-X., Yang, F. and Ji, W., Nature communications, 2014. **5**: p.4475
14. Fei, R. and Yang, L., Nano letters, 2014. **14**(5): pp. 2884-2889
15. Luo, Z., Maassen, J., Deng, Y., Du, Y., Garrelts, R.P., Lundstrom, M.S., Ye, P.D. and Xu, X., Nature communications, 2015. **6**: p.8572
16. Tao, J., Shen, W., Wu, S., Liu, L., Feng, Z., Wang, C., Hu, C., Yao, P., Zhang, H. and Pang, W., ACS nano, 2015. **9**(11): pp. 11362-11370
17. Zhu, J., Park, H., Chen, J.Y., Gu, X., Zhang, H., Karthikeyan, S., Wendel, N., Campbell, S.A., Dawber, M. and Du, X., Advanced Electronic Materials, 2016. **2**(5): p.1600040
18. Li, D., Jussila, H., Karvonen, L., Ye, G., Lipsanen, H., Chen, X. and Sun, Z., Scientific reports, 2015. **5**: p.15899
19. Li, L., Yu, Y., Ye, G.J., Ge, Q., Ou, X., Wu, H., Feng, D., Chen, X.H. and Zhang, Y., Nature nanotechnology, 2014. **9**(5): pp. 372-377
20. Wood, J.D., Wells, S.A., Jariwala, D., Chen, K.-S., Cho, E., Sangwan, V.K., Liu, X., Lauhon, L.J., Marks, T.J. and Hersam, M.C., Nano letters, 2014. **14**(12): pp. 6964-6970

21. Yuan, H., Liu, X., Afshinmanesh, F., Li, W., Xu, G., Sun, J., Lian, B., Curto, A.G., Ye, G. and Hikita, Y., Nature nanotechnology, 2015. **10**(8): pp. 707-713
22. Rodin, A., Carvalho, A. and Neto, A.C., Physical review letters, 2014. **112**(17): p.176801
23. Çakır, D., Sahin, H. and Peeters, F.M., Physical Review B, 2014. **90**(20): p.205421
24. Koenig, S.P., Doganov, R.A., Schmidt, H., Castro Neto, A. and Özyilmaz, B., Applied Physics Letters, 2014. **104**(10): p.103106
25. Schuster, R., Trinckauf, J., Habenicht, C., Knupfer, M. and Büchner, B., Physical review letters, 2015. **115**(2): p.026404
26. Roth, F., König, A., Fink, J., Büchner, B. and Knupfer, M., Journal of electron spectroscopy and related phenomena, 2014. **195**: pp. 85-95
27. Froitzheim, H., *Electron energy loss spectroscopy*, in *Electron spectroscopy for surface analysis*. 1977, Springer. pp. 205-250.
28. Williams, D.B. and Carter, C.B., *The transmission electron microscope*, in *Transmission electron microscopy*. 1996, Springer. pp. 3-17.
29. Nan, Z., Xiaoyu, J., Qiang, G., Yonghong, H. and Hui, M., Applied optics, 2009. **48**(35): pp. 6734-6739
30. Knill, E., Laflamme, R. and Milburn, G.J., nature, 2001. **409**(6816): pp. 46-52
31. Asahina, H. and Morita, A., Journal of Physics C: Solid State Physics, 1984. **17**(11): pp. 1839-1852
32. Liu, H., Neal, A.T., Zhu, Z., Xu, X., Tomanek, D., Ye, P.D. and Luo, Z., ACS nano, 2014. **8**(4): pp. 4033-4041
33. Pruessner, M.W., King, T.T., Kelly, D.P., Grover, R., Calhoun, L.C. and Ghodssi, R., Sensors and Actuators A: Physical, 2003. **105**(2): pp. 190-200
34. Frank, I., Tanenbaum, D.M., Van der Zande, A. and McEuen, P.L., Journal of Vacuum Science & Technology B: Microelectronics and Nanometer Structures Processing, Measurement, and Phenomena, 2007. **25**(6): pp. 2558-2561
35. Lee, C., Wei, X., Kysar, J.W. and Hone, J., science, 2008. **321**(5887): pp. 385-388
36. Wei, Q. and Peng, X., Applied Physics Letters, 2014. **104**(25): p.251915
37. Morita, A., Applied Physics A: Materials Science & Processing, 1986. **39**(4): pp. 227-242
38. Zhu, W., Perebeinos, V., Freitag, M. and Avouris, P., Physical Review B, 2009. **80**(23): p.235402
39. Chen, J.-H., Jang, C., Adam, S., Fuhrer, M., Williams, E. and Ishigami, M., Nature Physics, 2008. **4**(5): pp. 377-381
40. Blöchl, P.E., Physical Review B, 1994. **50**(24): p.17953
41. Kresse, G. and Joubert, D., Physical Review B, 1999. **59**(3): pp. 1758-1775
42. Bruzzone, S. and Fiori, G., Applied Physics Letters, 2011. **99**(22): p.222108
43. Takagi, S.-i., Toriumi, A., Iwase, M. and Tango, H., IEEE Transactions on Electron Devices, 1994. **41**(12): pp. 2357-2362
44. Fiori, G. and Iannaccone, G., Proceedings of the IEEE, 2013. **101**(7): pp. 1653-1669
45. Low, T., Rodin, A., Carvalho, A., Jiang, Y., Wang, H., Xia, F. and Neto, A.C., Physical Review B, 2014. **90**(7): p.075434

46. Engel, M., Steiner, M. and Avouris, P., Nano letters, 2014. **14**(11): pp. 6414-6417
47. Youngblood, N., Chen, C., Koester, S.J. and Li, M., Nature Photonics, 2015. **9**: pp. 247-252
48. Buscema, M., Groenendijk, D.J., Blanter, S.I., Steele, G.A., van der Zant, H.S. and Castellanos-Gomez, A., Nano letters, 2014. **14**(6): pp. 3347-3352
49. Yin, Z., Li, H., Li, H., Jiang, L., Shi, Y., Sun, Y., Lu, G., Zhang, Q., Chen, X. and Zhang, H., ACS nano, 2011. **6**(1): pp. 74-80
50. Lee, H.S., Min, S.-W., Chang, Y.-G., Park, M.K., Nam, T., Kim, H., Kim, J.H., Ryu, S. and Im, S., Nano letters, 2012. **12**(7): pp. 3695-3700
51. Lopez-Sanchez, O., Lembke, D., Kayci, M., Radenovic, A. and Kis, A., Nature nanotechnology, 2013. **8**(7): pp. 497-501
52. Pospischil, A., Furchi, M.M. and Mueller, T., Nature nanotechnology, 2014. **9**(4): pp. 257-261
53. Hu, P., Wang, L., Yoon, M., Zhang, J., Feng, W., Wang, X., Wen, Z., Idrobo, J.C., Miyamoto, Y. and Geohegan, D.B., Nano letters, 2013. **13**(4): pp. 1649-1654
54. Choi, W., Cho, M.Y., Konar, A., Lee, J.H., Cha, G.B., Hong, S.C., Kim, S., Kim, J., Jena, D. and Joo, J., Advanced Materials, 2012. **24**(43): pp. 5832-5836
55. Perea‐López, N., Elías, A.L., Berkdemir, A., Castro‐Beltran, A., Gutiérrez, H.R., Feng, S., Lv, R., Hayashi, T., López‐Urías, F. and Ghosh, S., Advanced Functional Materials, 2013. **23**(44): pp. 5511-5517
56. Bube, R.H., *Photoelectronic properties of semiconductors*. 1992: Cambridge University Press.
57. Hu, P., Wen, Z., Wang, L., Tan, P. and Xiao, K., ACS nano, 2012. **6**(7): pp. 5988-5994
58. Chui, C.O., Okyay, A.K. and Saraswat, K.C., IEEE Photonics Technology Letters, 2003. **15**(11): pp. 1585-1587
59. Mueller, T., Xia, F. and Avouris, P., Nature Photonics, 2010. **4**(5): pp. 297-301
60. Freitag, M., Low, T., Xia, F. and Avouris, P., Nature Photonics, 2013. **7**(1): pp. 53-59
61. Lv, H., Lu, W., Shao, D. and Sun, Y., Physical Review B, 2014. **90**(8): p.085433
62. Qin, G., Yan, Q.-B., Qin, Z., Yue, S.-Y., Cui, H.-J., Zheng, Q.-R. and Su, G., Scientific reports, 2014. **4**: p.6946
63. Fei, R., Faghaninia, A., Soklaski, R., Yan, J.-A., Lo, C. and Yang, L., Nano letters, 2014. **14**(11): pp. 6393-6399
64. Tkachenko, N.V., *Optical spectroscopy: methods and instrumentations*. 2006: Elsevier.
65. Lin, H.N., Stoner, R., Maris, H. and Tauc, J., Journal of applied physics, 1991. **69**(7): pp. 3816-3822
66. O’Hara, K., Hu, X. and Cahill, D.G., Journal of applied physics, 2001. **90**(9): pp. 4852-4858
67. Thomsen, C., Grahn, H.T., Maris, H.J. and Tauc, J., Physical Review B, 1986. **34**(6): pp. 4129-4138
68. Thomsen, C., Grahn, H., Maris, H. and Tauc, J., Optics communications, 1986. **60**(1-2): pp. 55-58

69. Chiritescu, C., *Ultra low thermal conductivity in layered disordered crystalline materials*. 2010, University of Illinois at Urbana-Champaign.
70. Köpf, M., Eckstein, N., Pfister, D., Grotz, C., Krüger, I., Greiwe, M., Hansen, T., Kohlmann, H. and Nilges, T., Journal of Crystal Growth, 2014. **405**: pp. 6-10
71. Cahill, D.G., Review of scientific instruments, 2004. **75**(12): pp. 5119-5122
72. Christofferson, J. and Shakouri, A., Review of scientific instruments, 2005. **76**(2): p.024903
73. Kendig, D., 2013
74. Cahill, D.G. and Allen, T.H., Applied Physics Letters, 1994. **65**(3): pp. 309-311
75. Manifacier, J., Gasiot, J. and Fillard, J., Journal of Physics E: Scientific Instruments, 1976. **9**(11): pp. 1002-1004
76. Matsuda, O., Wright, O., Hurley, D., Gusev, V. and Shimizu, K., Physical review letters, 2004. **93**(9): pp. 095501: p.095501
77. White, R.M., Journal of applied physics, 1963. **34**(12): pp. 3559-3567
78. Eesley, G.L., Clemens, B.M. and Paddock, C.A., Applied Physics Letters, 1987. **50**(12): pp. 717-719
79. Brillouin, L., Ann. Phys.(Paris), 1922. **17**(21): pp. 88-122
80. Island, J.O., Steele, G.A., van der Zant, H.S. and Castellanos-Gomez, A., 2D Materials, 2015. **2**(1): p.011002
81. Ma, W., Miao, T., Zhang, X., Kohno, M. and Takata, Y., The Journal of Physical Chemistry C, 2015. **119**(9): pp. 5152-5159
82. Still, T., *High frequency acoustics in colloid-based meso-and nanostructures by spontaneous Brillouin light scattering*. 2009, Johannes Gutenberg-Universität Mainz.
83. Liu, J., Choi, G.-M. and Cahill, D.G., Journal of applied physics, 2014. **116**(23): pp. 233107
84. Jang, H., Wood, J.D., Ryder, C.R., Hersam, M.C. and Cahill, D.G., Advanced Materials, 2015. **27**(48): pp. 8017-8022
85. Matatagui, E., Thompson, A. and Cardona, M., Physical Review, 1968. **176**(3): pp. 950-960
86. Flores, E., Ares, J.R., Castellanos-Gomez, A., Barawi, M., Ferrer, I.J. and Sánchez, C., Applied Physics Letters, 2015. **106**(2): pp. 022102
87. Paddock, C.A. and Eesley, G.L., Journal of applied physics, 1986. **60**(1): pp. 285-290
88. Capinski, W.S. and Maris, H.J., Review of scientific instruments, 1996. **67**(8): pp. 2720-2726
89. Manzoni, C., Polli, D. and Cerullo, G., Review of scientific instruments, 2006. **77**(2): pp. 023103
90. Antonelli, G.A., Perrin, B., Daly, B.C. and Cahill, D.G., MRS bulletin, 2006. **31**(08): pp. 607-613
91. Tritt, T.M., *Thermal conductivity: theory, properties, and applications*. 2005: Springer Science & Business Media.